

1  
2 **Role of the circulation on the anthropogenic CO<sub>2</sub> inventory in the North-East Atlantic: a**  
3 **climatological analysis**

4  
5 **L.I. Carracedo<sup>1, 2</sup>, F.F. Pérez<sup>2</sup>, M. Gilcoto<sup>2</sup>, A. Velo<sup>2</sup>, A. Padín<sup>2</sup>, G. Rosón<sup>1</sup>**

6  
7 <sup>1</sup> Physical Oceanography Group (GOFUVI), Faculty of Marine Sciences, Universidade de Vigo  
8 (Spain), Campus Lagoas-Marcosende, 36200, Vigo, Spain, Tel: (+34) 986 81 40 70.

9 <sup>2</sup> Oceanology Group, Instituto de Investigaciones Marinas, CSIC, Eduardo Cabello 6, 36208 Vigo,  
10 Spain, Tel: (+34) 986 231 930.

11  
12 Corresponding author: Lidia I. Carracedo Segade ([lcarracedo@uvigo.es](mailto:lcarracedo@uvigo.es))

13 **Keywords:** Anthropogenic CO<sub>2</sub>; Carbon storage; Air-sea CO<sub>2</sub> uptake; Water masses;  
14 Overturning; Gulf of Cadiz; North-East Atlantic

15 **Highlights:**

- 16 • North-East Atlantic climatology-based C<sub>ant</sub> storage rate of  $0.020 \pm 0.003$  Pg-C yr<sup>-1</sup>  
17 • C<sub>ant</sub> import ( $43 \pm 14$  kmol s<sup>-1</sup>) driven by the upper overturning circulation limb  
18 • Net C<sub>ant</sub> advection contributes to 60% of the C<sub>ant</sub> storage rate  
19 • Atmospheric C<sub>ant</sub> uptake contributes to 40% of the C<sub>ant</sub> storage rate  
20 •  $78 \pm 30\%$  of the annual air-sea CO<sub>2</sub> uptake is of anthropogenic nature ( $21 \pm 10$  kmol s<sup>-1</sup>)  
21  
22  
23

## 24 Abstract

25 Climatology-based storage rate of anthropogenic CO<sub>2</sub> ( $C_{\text{ant}}$ , referred to year 2000) in the  
26 North-East Atlantic ( $53 \pm 9 \text{ kmol s}^{-1}$ ,  $0.020 \pm 0.003 \text{ Pg-C yr}^{-1}$ ) is described on annual mean terms.  
27  $C_{\text{ant}}$  advection ( $32 \pm 14 \text{ kmol s}^{-1}$ ) occurs mostly in the upper 1800 m and contributes to 60% of the  
28  $C_{\text{ant}}$  storage rate. The Azores and Portugal Currents act as ' $C_{\text{ant}}$  streams' importing  $389 \pm 90 \text{ kmol}$   
29  $\text{s}^{-1}$ , most of which recirculates southwards with the Canary Current ( $-214 \pm 34 \text{ kmol s}^{-1}$ ). The  
30 Azores Counter Current ( $-79 \pm 36 \text{ kmol s}^{-1}$ ) and the northward-flowing Mediterranean Water  
31 advective branch ( $-31 \pm 12 \text{ kmol s}^{-1}$ ) comprise secondary  $C_{\text{ant}}$  export routes. By means of  $C_{\text{ant}}$   
32 transport decomposition, we find horizontal circulation to represent 11% of the  $C_{\text{ant}}$  storage rate,  
33 while overturning circulation is the main driver (48% of the  $C_{\text{ant}}$  storage rate). Within the domain  
34 of this study, overturning circulation is a key mechanism by which  $C_{\text{ant}}$  in the upper layer (0-500  
35 dbar) is drawdown ( $74 \pm 14 \text{ kmol s}^{-1}$ ) to intermediate levels (500-2000 dbar), and entrained ( $37 \pm$   
36  $7 \text{ kmol s}^{-1}$ ) into the Mediterranean Outflow Water to form Mediterranean Water. This newly  
37 formed water mass partly exports  $C_{\text{ant}}$  to the North Atlantic at a rate of  $-39 \pm 9 \text{ kmol s}^{-1}$  and partly  
38 contributes to the  $C_{\text{ant}}$  storage in the North-East Atlantic (with up to  $0.015 \pm 0.006 \text{ Pg-C yr}^{-1}$ ).  
39 Closing the  $C_{\text{ant}}$  budget, 40% of the  $C_{\text{ant}}$  storage in the North-East Atlantic is attributable to  
40 anthropogenic CO<sub>2</sub> uptake from the atmosphere ( $21 \pm 10 \text{ kmol s}^{-1}$ ).

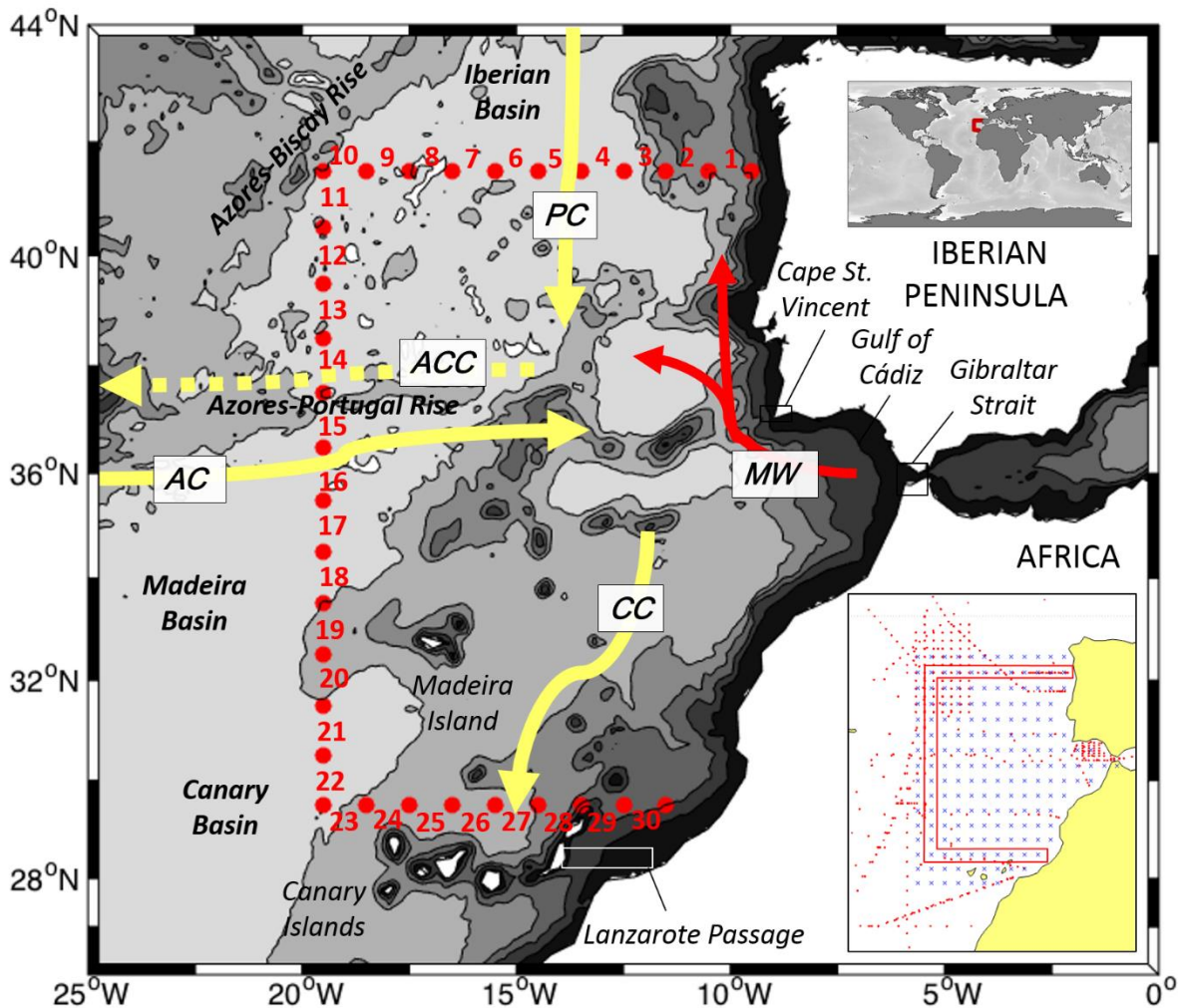
## 41 1 Introduction

42 Human activities such as fossil fuel burning or deforestation have emitted large amounts of  
43 CO<sub>2</sub> into the atmosphere (anthropogenic CO<sub>2</sub>,  $C_{\text{ant}}$ ) since the Industrial Revolution (1750s),  
44 thereby increasing the global atmospheric CO<sub>2</sub> content (Stocker et al., 2013). The ocean plays an  
45 important role in the global carbon budget, acting as a net CO<sub>2</sub> sink (Watson et al., 2009). Global  
46 model-based studies refer to a mean (2004–2013) CO<sub>2</sub> ocean uptake rate of  $2.6 \pm 0.5 \text{ Pg-C yr}^{-1}$  (Le  
47 Quéré et al., 2015). Of the world's oceans, the North Atlantic represents only 13% of the global  
48 ocean area, but yet accounts for about one-third of the contemporary global air-to-sea annual CO<sub>2</sub>  
49 flux and contains the largest  $C_{\text{ant}}$  inventory (Sabine et al., 2004). The Atlantic meridional  
50 overturning circulation plays a strong part on it by driving the variability of the  $C_{\text{ant}}$  transport from  
51 subtropics to the subpolar North Atlantic (Zunino et al., 2014) and by favoring the CO<sub>2</sub> sink  
52 through deep water mass formation (Steinfeldt et al., 2009). Actually, Pérez et al. (2013) suggested  
53 that changes in the strength of the overturning circulation in the North Atlantic correlated  
54 positively with the  $C_{\text{ant}}$  storage rate, so the observed reduction of the overturning could be leading  
55 to a decrease of CO<sub>2</sub> storage capacity in the subpolar North Atlantic. Therefore, quantifying the  
56 transport and storage of  $C_{\text{ant}}$  in the oceans is relevant for predicting its future evolution in a world  
57 of growing CO<sub>2</sub> emissions (Rhein et al., 2013).

58 More regionally, in the North-East Atlantic (Fig. 1), there is also an overturning cell  
59 primarily responsible for the transfer of  $C_{\text{ant}}$  from surface to deeper levels (Álvarez et al., 2005).  
60 In this region, the Strait of Gibraltar yields a unique water mass exchange between salty  
61 Mediterranean Outflow Water and East North Atlantic Central Water. The spilling down of  
62 Mediterranean Outflow Water towards the Atlantic generates an area of convergence and  
63 subduction (overturning circulation) west off the Strait, in the Gulf of Cadiz (Fig. 1). There, central  
64 waters are entrained and mixed with Mediterranean Outflow Water to form Mediterranean Water  
65 (MW) (van Aken, 2000; Fusco et al., 2008; Carracedo et al., 2016), the salty water mass that  
66 ultimately spreads over the entire North Atlantic. Previous studies have focused on the North-East  
67 Atlantic as a potential sink for  $C_{\text{ant}}$  (Ríos et al., 2001; Álvarez et al., 2005; Pérez et al., 2010; Fajar

68 et al., 2012): evaluating the influence of the MW in the CO<sub>2</sub> inventories of the North Atlantic  
 69 (Álvarez et al., 2005); quantifying the C<sub>ant</sub> storage in the Gulf of Cadiz (Ait-Ameur and Goyet,  
 70 2006; Flecha et al., 2012; Ribas-Ribas et al., 2011); or computing the CO<sub>2</sub> exchange in the Strait  
 71 of Gibraltar (Huertas et al., 2009).

72 This paper aims to provide a description of the mean annual climatological C<sub>ant</sub> transport in  
 73 the North-East Atlantic across a box defined west of the Gibraltar Strait (Fig. 1), based on  
 74 GLODAPv2 cruise bottle data (Key et al., 2015; Olsen et al., 2016) and the World Ocean Atlas  
 75 2009 climatological database (WOA09, Boyer et al., 2009). We study the contribution of the  
 76 horizontal and overturning circulation to C<sub>ant</sub> storage and, as a residual term of the C<sub>ant</sub> budget, we  
 77 also provide the anthropogenic contribution to air-sea CO<sub>2</sub> exchange. We first present the data and  
 78 methods to calculate C<sub>ant</sub> concentrations (section 2.1), transports (section 2.2) and storage rates  
 79 in/into/within the box (section 2.3); next, we describe the annual mean C<sub>ant</sub> spatial distribution  
 80 (section 3.1) and the part taken by horizontal circulation in C<sub>ant</sub> redistribution (section 3.2); we  
 81 then examine and discuss the C<sub>ant</sub> budget and the main role played by the overturning circulation  
 82 (section 3.3); and, finally, we present a summary and concluding remarks in section 4.



83 **Figure 1.** Study area, showing main bathymetric features. Yellow arrows indicate the main surface  
 84 currents (PC, Portugal Current; AC, Azores Current; CC, Canary Current); yellow dotted arrow  
 85

86 the subsurface Azores Counter Current (ACC); and red arrows the main spreading paths for  
87 Mediterranean Water (MW). Red dots mark WOA09-Box station-like positions and red numbers  
88 1 to 30 the station pairs as used for velocity estimates (see section 2.2 for details). Inset figures:  
89 upper panel, world map location; lower panel, GLODAPv2 bottle data (red dots), WOA09 grid  
90 (blue crosses) and WOA09-Box section (red polygon).

## 91 **2 Materials and Methods**

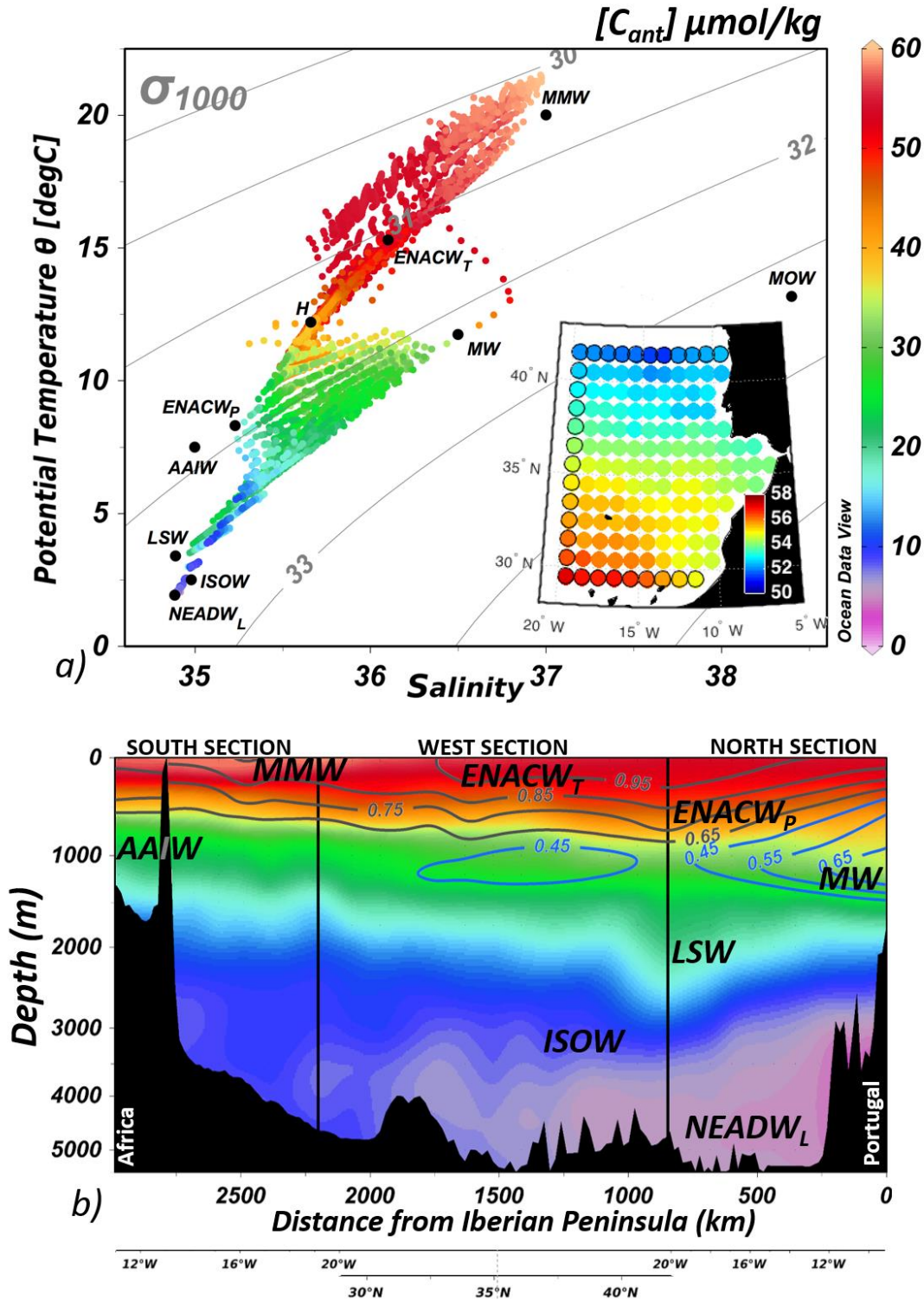
### 92 2.1 $C_{\text{ant}}$ concentration

93  $C_{\text{ant}}$  concentrations were estimated by means of a back-calculation technique, the  $\phi_{\text{CT}}^0$   
94 method (Vázquez-Rodríguez et al., 2009a, 2009b, 2012) (Appendix A.1), which involves the  
95 carbonate system variables (total inorganic carbon, total alkalinity and pH) as input data. In this  
96 study, these required data were obtained from the GLODAPv2 ocean bottle database (Key et al.,  
97 2015; Olsen et al., 2016). A total of 10023 observations were used (Fig. 1, bottom inset figure, red  
98 dots).  $C_{\text{ant}}$  estimates were scaled from their original cruise year to year 2000, for analogy with the  
99 sea-air  $\text{CO}_2$  flux climatology of Takahashi et al. (2009) (see section 2.4), using the transient steady  
100 state approach (Tanhua et al., 2006) (see Appendix A.1).

101 Once estimated,  $C_{\text{ant}}$  values were interpolated to the 5574 nodes of the  $1^\circ \times 1^\circ \times 33$  levels  
102 WOA09 grid resolution of the World Ocean Atlas 2009 (WOA09) database (Boyer et al., 2009)  
103 (Fig. 1, bottom inset figure, blue crosses). The interpolation was done using a WMP (Water Masses  
104 Properties) multi-parametric interpolation method (Velo et al., 2010) based on WOA09 physical  
105 (potential temperature  $\theta$ , and salinity  $S$ ) and biogeochemical tracers (“NO” and “PO”, where  $\text{NO}$   
106 =  $9 \times \text{nitrate} + \text{oxygen}$ ,  $\text{PO} = 135 \times \text{phosphate} + \text{oxygen}$  (Anderson and Sarmiento, 1994; Broecker,  
107 1974; Takahashi et al., 1985)). The WMP method consists in an inverse distance weighting  
108 algorithm in which the distance is taken in the multi-parametric space from each WOA09 node.  
109 Those  $C_{\text{ant}}$  (ref. 2000) samples with higher associated multi-parametric distance are down-  
110 weighted while those closer to the climatologic mean WOA09 nodes are up-weighted. Therefore,  
111 the method pushes the final  $C_{\text{ant}}$  interpolation to a solution closer to the WOA09 climatologic  
112 mean, somehow reducing the time discrepancies present on the GLODAPv2 ancillary parameters.

113 Next, 31 adjacent WOA09 grid nodes were selected as hydrographic “stations” (vertical  
114 profiles) so that they formed an enclosed box west of the Gibraltar Strait, as in Carracedo et al.  
115 (2014) (referred to as the WOA09-Box hereafter) (Fig. 1). This box was approximately coincident  
116 with the 2009 CAIBEX (Shelf–Ocean Exchanges in the Canaries-Iberian Large Marine Ecosystem  
117 Project) cruise track (CAIBOX-2009) (Carracedo et al., 2015; Fajar et al., 2012; Lønborg and  
118 Álvarez-Salgado, 2014). In Fig. 2b,  $C_{\text{ant}}$  concentrations for the WOA09-Box limits are shown. For  
119 further illustration, spatial distributions of the  $C_{\text{ant}}$  averaged concentrations (anomalies) at three  
120 different depth ranges (0-150, 150-800 and 800-1200 m) are shown in Appendix B (Fig. B1).





121

122 **Figure 2.** a)  $\theta/S$  diagram of the surface-to-bottom WOA09-Box enclosed data. Color scale  
 123 represents the concentration of anthropogenic  $\text{CO}_2$  ( $C_{\text{ant}}$ , in  $\mu\text{mol kg}^{-1}$ ). Black dots denote the  
 124 source water types of the main water masses present in the region: MMW, Madeira Mode Water;  
 125 ENACW<sub>T</sub>, Subtropical East North Atlantic Central Water; ENACW<sub>P</sub>, Subpolar East North

126 Atlantic Central Water; MW, Mediterranean Water; MOW, Mediterranean Outflow Water;  
 127 AAIW, Antarctic Intermediate Water; LSW, Labrador Sea Water; ISOW, Iceland–Scotland  
 128 Overflow Water; NEADW<sub>L</sub>, Lower North-East Atlantic Deep Water. Inset figure: horizontal  
 129 distribution of  $C_{ant}$  ( $\mu\text{mol kg}^{-1}$ ) averaged in the first 150 m of the water column. *b*) Vertical  
 130 distribution of  $C_{ant}$  ( $\mu\text{mol kg}^{-1}$ ) along the South-West-North limits of the WOA09-Box (section  
 131 distance refers to accumulated distance from Portugal to Africa). Note color scale is the same as  
 132 for Fig. 1a. Dark grey isolines correspond to central waters (MMW+ENACW<sub>T</sub>+ENACW<sub>P</sub>)  
 133 contribution (per one percentage). Dark blue isolines refer to MW contribution (per one  
 134 percentage).

## 135 2.2 $C_{ant}$ transports

136 The transport of  $C_{ant}$  perpendicular to the WOA09-Box,  $TC_{ant}$ , is computed as:

$$137 \quad TC_{ant} = \sum_{j=stp1}^{stp2} \Delta x_j \int_{z_1}^{z_2} \rho_j C_{antj} v_j dz, \quad (1)$$

138 For each station pair  $j$ ,  $\rho_j$  is seawater density profile ( $\text{kg m}^{-3}$ ),  $C_{antj} = C_{antj}(z)$  is the  $C_{ant}$   
 139 concentration profile ( $\mu\text{mol kg}^{-1}$ ) and  $v_j = v_j(z)$  is the (absolute) velocity profile ( $\text{m s}^{-1}$ ).  $\Delta x$  is the  
 140 horizontal coordinate (station pair spacing along the perimeter of the WOA-Box, in m), with  $stp1$   
 141 and  $stp2$  referring to two different station pairs. Station pair notation refers to the mid-point  
 142 between the 31 WOA09 nodes.  $z$  is the vertical coordinate (depth, in m), with  $z_1$  and  $z_2$  referring  
 143 to two different depths. For the  $C_{ant}$  transport across the limits of the whole domain ( $stp1=1$ ,  
 144  $stp2=30$ ,  $z_1$ =surface,  $z_2$ =bottom), we will refer to  $T_{Box}C_{ant}$ . Note equation (1) expresses the  
 145 horizontal summation of transports per station pair integrated in depth (1-m resolution profiles).  
 146 For the across-section absolute velocity field,  $v$ , we used the estimate by Carracedo et al. (2014),  
 147 solved by means of a two-dimensional geostrophic inverse ocean model (Mercier, 1986). Briefly,  
 148 the inverse box model was applied to the three oceanic transects selected from the annual WOA09  
 149 dataset. The model, which includes the surface Ekman transport, solves for the reference-level  
 150 velocities that best satisfy the conservation of volume, salt and heat (and/or other *a priori* specified  
 151 constraints). Afterwards, the absolute velocity field is computed as the sum of that estimation of  
 152 velocities at the reference level, and the relative velocities calculated from the density field (i.e.,  
 153 geostrophic velocities obtained by the thermal wind equations). For further details about the  
 154 method used to compute the absolute volume transports and description of the large-scale gyre  
 155 circulation in the North-East Atlantic region (Azores Current; Azores Counter Current; Canary  
 156 Current; Portugal Current; and Iberian Poleward Current), we refer the reader to Carracedo et al.  
 157 (2014). Hereafter, positive (negative) transports indicate flows into (out of) the box.

158 Finally, to further assess the elements of the circulation that influence the advection of  $C_{ant}$ ,  
 159  $TC_{ant}$  was decomposed into three components (Álvarez et al., 2005): a throughflow or barotropic  
 160 term due to the net transport across the box and the section-averaged  $C_{ant}$  ( $T_{baro}C_{ant}$ ); a baroclinic  
 161 or overturning term due to the horizontally averaged vertical structure of the velocity and  $C_{ant}$   
 162 fields ( $T_{over}C_{ant}$ ); and finally, a horizontal term due to the residual velocities and residual  $C_{ant}$   
 163 concentrations after the barotropic and overturning components have been subtracted that is  
 164 associated with the gyre circulation ( $T_{horiz}C_{ant}$ ). According to that,  $TC_{ant}$  was split as:

$$165 \quad TC_{ant} = T_{baro}C_{ant} + T_{over}C_{ant} + T_{horiz}C_{ant}$$

$$TC_{ant} = \rho \langle C_{ant} \rangle V_0 \int L(z) dz + \rho \int \langle C_{ant} \rangle (z) \langle v \rangle (z) L(z) dz + \rho \sum_{j=stp1}^{stp2} \Delta x_j \int C_{antj}'(z) v_j'(z) L_j(z) dz \quad (2)$$

where  $\rho$  refers to the mean seawater density,  $V_0$  is the section-averaged velocity ( $V_0 = T_{Box}/A$ , with  $T_{Box}$  being the net volume transport across the section, i.e., the North, West and south bounds of the box, and  $A$  the total area of the section).  $\langle v \rangle (z)$  is the mean vertical profile of the velocity anomalies ( $v(x,z) - V_0$ ).  $v_j'(z)$  represents the deviations from the mean vertical profile ( $v_j'(z) = v_j(z) - \langle v \rangle (z)$ ). For  $C_{ant}$ ,  $\langle C_{ant} \rangle$  represents the section mean,  $\langle C_{ant} \rangle (z)$  is the mean vertical profile of  $C_{ant}$  anomalies ( $C_{ant}(x,z) - \langle C_{ant} \rangle$ ), and  $C_{antj}'(z)$  are the deviations from the corresponding mean vertical profile ( $C_{antj}'(z) = C_{antj}(z) - \langle C_{ant} \rangle (z)$ ).

In order to evaluate the contribution of central waters and MW to the  $C_{ant}$  budget, we used the water mass fractions solved by Carracedo et al. (2014), by means an Optimum MultiParameter mixing analysis (OMP analysis, Tomczak, 1981; Pardo et al., 2012).  $c_{wmj} = c_{wmj}(z)$  is the water mass contribution profile with values in the range 0–1, that reflects the proportion of a given water mass involved in the mixing process (0 indicates no contribution and 1 100% contribution). By combining  $C_{ant}$  transports with water mass fractions, we can estimate the relative contribution of each water mass as follows:

$$(TC_{ant})_{wm} = \sum_{j=stp1}^{stp2} \Delta x_j \int_{z1}^{z2} \rho_j C_{antj} v_j c_{wmj} dz \quad (3)$$

Likewise, to determine the MW or central waters contribution to the  $C_{ant}$  transport decomposition (Eq. 2), each component ( $T_{net}C_{ant}$ ,  $T_{over}C_{ant}$ ,  $T_{horiz}C_{ant}$ ) was multiplied by the respective contribution matrix ( $c_{mw}$ , for MW; or  $c_{cw}$ , for central waters). Central waters and MW contribution are shown in Fig. 2b. Note in this study, central waters account for the sum contribution of three end-members, as solved by Carracedo et al. (2014): the Madeira Mode Water (MMW) and the Subtropical and Subpolar East North Atlantic Central Water (ENACW<sub>T</sub> and ENACW<sub>P</sub>, respectively) (Fig. 2a, Table A2).

### 2.3 Calculation of $C_{ant}$ budget

In order to study the  $C_{ant}$  budget in the region, the inventory of  $C_{ant}$  ( $C_{ant} inventory$ ) was computed by integrating  $C_{ant}$  concentrations vertically and horizontally, considering all WOA09 nodes inside the box (Fig. 1, inset figure):

$$C_{ant} inventory = \iiint C_{ant} dx dy dz \quad (4)$$

$C_{ant} inventory$  can be given as a total inventory, in Pg-C (1 Pg-C=1 GtC), or, alternatively, as specific inventory (per unit area), in molC m<sup>-2</sup>. Provided the transient steady state assumption (Tanhua et al., 2006; Keeling and Bolin, 2010), the time derivative of  $C_{ant}$  ( $C_{ant} storage rate$ ) can be obtained by multiplying the  $C_{ant} inventory$  by the annual  $C_{ant}$  rate of increase  $k_t$  ( $k_t = 0.0169 \pm 0.0010$  y<sup>-1</sup>, Steinfeldt et al. (2009)) Therefore,

$$C_{ant} storage rate = k_t C_{ant} inventory \quad (5)$$

201 The transient steady state assumption implies that through the whole water column,  $C_{\text{ant}}$  will  
 202 increase over time at a rate that is proportional to the  $C_{\text{ant}}$  increase in the mixed layer. In a recent  
 203 study carried out in the Equatorial Atlantic Ocean, Fajar et al. (2015) found that the estimated  $C_{\text{ant}}$   
 204 storage rates were consistent, within the uncertainties, to those based on the steady state  
 205 assumption. This supports the feasibility of using this premise in a climatological data-based  
 206 framework. As for the  $C_{\text{ant}}$  inventory, note the  $C_{\text{ant}}$  storage rate can also be given as specific storage  
 207 rate (per unit area), in  $\text{molC m}^{-2} \text{y}^{-1}$ ; or as total storage rate, in  $\text{Pg-C y}^{-1}$  or  $\text{kmol s}^{-1}$ .

208 The final  $C_{\text{ant}}$  budget within any oceanic basin will result from the balance between lateral  
 209 advection (box across-boundaries' transports), air-sea fluxes and the storage rate in the form:

$$210 \quad C_{\text{ant}} \text{ storage rate} = T_{\text{Box}}C_{\text{ant}} + T_{\text{Strait}}C_{\text{ant}} + F_{\text{Air-sea}}C_{\text{ant}} \quad (6)$$

211 where  $C_{\text{ant}}$  storage rate is estimated with Eq. (5).  $T_{\text{Box}}C_{\text{ant}}$  refers to the net transport of  $C_{\text{ant}}$  across  
 212 the northern, western and southern limits of WOA09-Box, as estimated from Eq. (1).  $T_{\text{Strait}}C_{\text{ant}}$   
 213 refers to the net transport of  $C_{\text{ant}}$  across the Strait of Gibraltar. For  $T_{\text{Strait}}C_{\text{ant}}$ , we used the estimate  
 214 of Huertas et al. (2009), who calculated a 2-year mean net flux of  $C_{\text{ant}}$  towards the Mediterranean  
 215 basin of  $4.20 \pm 0.04 \text{ Tg C yr}^{-1}$ , that is,  $11 \pm 1 \text{ kmol s}^{-1}$ . This value is in agreement with Álvarez et  
 216 al. (2005). Note that according to our sign convention (fluxes out of WOA09-Box take a negative  
 217 sign)  $T_{\text{Strait}}C_{\text{ant}}$  becomes  $-11 \pm 1 \text{ kmol s}^{-1}$ . Finally,  $F_{\text{Air-sea}}C_{\text{ant}}$  refers to the net air-sea anthropogenic  
 218  $\text{CO}_2$  flux in the region. Among the four terms of the equation,  $F_{\text{Air-sea}}C_{\text{ant}}$  is the one introducing a  
 219 higher uncertainty to the budget estimate, so that this term was isolated from Eq. (6), considered  
 220 an unknown and, therefore, became our final target.

## 221 2.4 Air-sea $\text{CO}_2$ exchange

222 In order to assess the  $C_{\text{ant}}$  budget depicted by our results, the  $F_{\text{Air-sea}}C_{\text{ant}}$  estimate (Eq. 6) was  
 223 compared to the total air-sea  $\text{CO}_2$  exchange in the region ( $F_{\text{Air-sea}}\text{CO}_2$ ). The annual average of the  
 224 monthly air-sea  $\text{CO}_2$  fluxes was obtained from the global climatology of Takahashi et al. (2009).  
 225 Their monthly  $F_{\text{Air-sea}}\text{CO}_2$  estimate is the product of the sea-air  $\text{pCO}_2$  difference ( $\Delta\text{pCO}_2$ , in  $\mu\text{atm}$ ;  
 226 see Fig. B2 in Appendix B) and the air-sea gas transfer rate ( $Tr$ , in  $\text{kmol m}^{-2} \text{month}^{-1} \mu\text{atm}^{-1}$ ), both  
 227 referenced to year 2000. For more details about the source datasets required for the monthly  
 228 climatologic air-sea  $\text{CO}_2$  flux calculation and/or for  $Tr$  formulation, the reader is referred to  
 229 Takahashi et al. (2009). From their original spatial resolution of  $4^\circ$  (latitude)  $\times$   $5^\circ$  (longitude), we  
 230 spatially interpolated the data to the WOA09 grid. Finally, we averaged the flux estimates  
 231 considering the whole WOA09-Box surface ( $1.36 \times 10^{12} \text{ m}^2$ ) so that obtaining the annual mean  
 232 air-sea  $\text{CO}_2$  exchange within our domain of study.

## 233 3 Results and Discussion

### 234 3.1 $C_{\text{ant}}$ distribution

235 The  $C_{\text{ant}}$  distribution shows the characteristic vertical decreasing gradient in depth (Fig. 2b).  
 236 Maximum concentrations of  $C_{\text{ant}}$  ( $\sim 60 \mu\text{mol kg}^{-1}$ ) are found in the first 150 m of the water column,  
 237 where the highest proportion of East North Atlantic Central Water is present (Carracedo et al.,  
 238 2014). Within this layer, the horizontal  $C_{\text{ant}}$  distribution (Fig. 2a, inset figure) shows a marked  
 239 latitudinal gradient, with increasing concentration towards the equator. Lower  $C_{\text{ant}}$  values off the



240 African coast are due to the year-round upwelling of deep waters with low  $C_{ant}$  (Speth et al., 1978).  
 241 Below the upper layer ( $>150$  m),  $C_{ant}$  decreases slowly down to 1200 m (Fig. 2b), with a sharper  
 242 gradient in the southern side of the box compared to the northern side. That relates to the presence  
 243 of Antarctic Intermediate Water with lower  $C_{ant}$  content ( $\sim 22 \mu\text{mol kg}^{-1}$ ) south of the region, in  
 244 contrast to the occurrence, further north, of MW with a higher  $C_{ant}$  ( $30\text{-}35 \mu\text{mol kg}^{-1}$ ). The relative  
 245 maximum at the 2000-m level ( $\sim 20 \mu\text{mol kg}^{-1}$ ) is linked to the Labrador Sea Water entering the  
 246 box through its north-west corner (Carracedo et al., 2014). At depths below 2000m,  $C_{ant}$   
 247 concentration is low ( $<15 \mu\text{mol kg}^{-1}$ ) but still noticeable, due to the deep penetration of  $C_{ant}$  in the  
 248 high-latitude regions of the North Atlantic by the formation and subsequent spreading of the North  
 249 Atlantic Deep Water (Woosley et al., 2016). The lowest  $C_{ant}$  values are found in the southern corner  
 250 of the box, related to the presence of the deepest component of the North-East Atlantic Deep Water,  
 251 the remains of the southern-ocean origin Antarctic Bottom water (Carracedo et al., 2014).

### 252 3.2 Role of the horizontal advection in the $C_{ant}$ distribution

253 The advective  $C_{ant}$  transports across the limits of WOA09-Box are shown in Fig. 3a. We  
 254 obtained a net flux of  $43 \pm 14 \text{ kmol s}^{-1}$  ( $T_{Box}C_{ant}$ , Eq. 1). For a similar box in the same region, but  
 255 built by combination of three different non-synoptic cruise sections, Álvarez et al. (2005) obtained  
 256 a net  $C_{ant}$  transport of  $66 \pm 14 \text{ kmol s}^{-1}$ . Although being higher the latter, neither value is statistically  
 257 distinguishable within the uncertainties. It is notable, however, that quasi-synoptic cruise-based  
 258 tracer transport estimates are affected by mesoscale and seasonal variability and may not  
 259 necessarily be representative of an annual climatology.

260 As depicted in Fig. 3a,  $C_{ant}$  transport is stronger in the upper 1500 m. In fact, the 0-1500 m  
 261 depth range accounts for more than 90% of the  $C_{ant}$  advection. This underlines the  
 262 upper/intermediate circulation as responsible for  $C_{ant}$  redistribution and transport into/out of the  
 263 region. By estimating  $TC_{ant}$  of the main currents (see integration limits by currents in Table 1), we  
 264 find that the Canary Current is the main current exporting  $C_{ant}$  out of the box ( $-214 \pm 34 \text{ kmol s}^{-1}$ ),  
 265 while the Azores Current is the main input source ( $314 \pm 88 \text{ kmol s}^{-1}$ ). From the total net  $389 \pm 90$   
 266  $\text{kmol s}^{-1}$  of  $C_{ant}$  being imported by Portugal and Azores Currents, around 20% recirculates  
 267 westwards and northwards, within the Azores Counter Current ( $-79 \pm 36 \text{ kmol s}^{-1}$ ) and the Iberian  
 268 Poleward Current ( $-11 \pm 3 \text{ kmol s}^{-1}$ ), respectively; while more than a half (55%) is transported  
 269 southwards by the Canary Current.

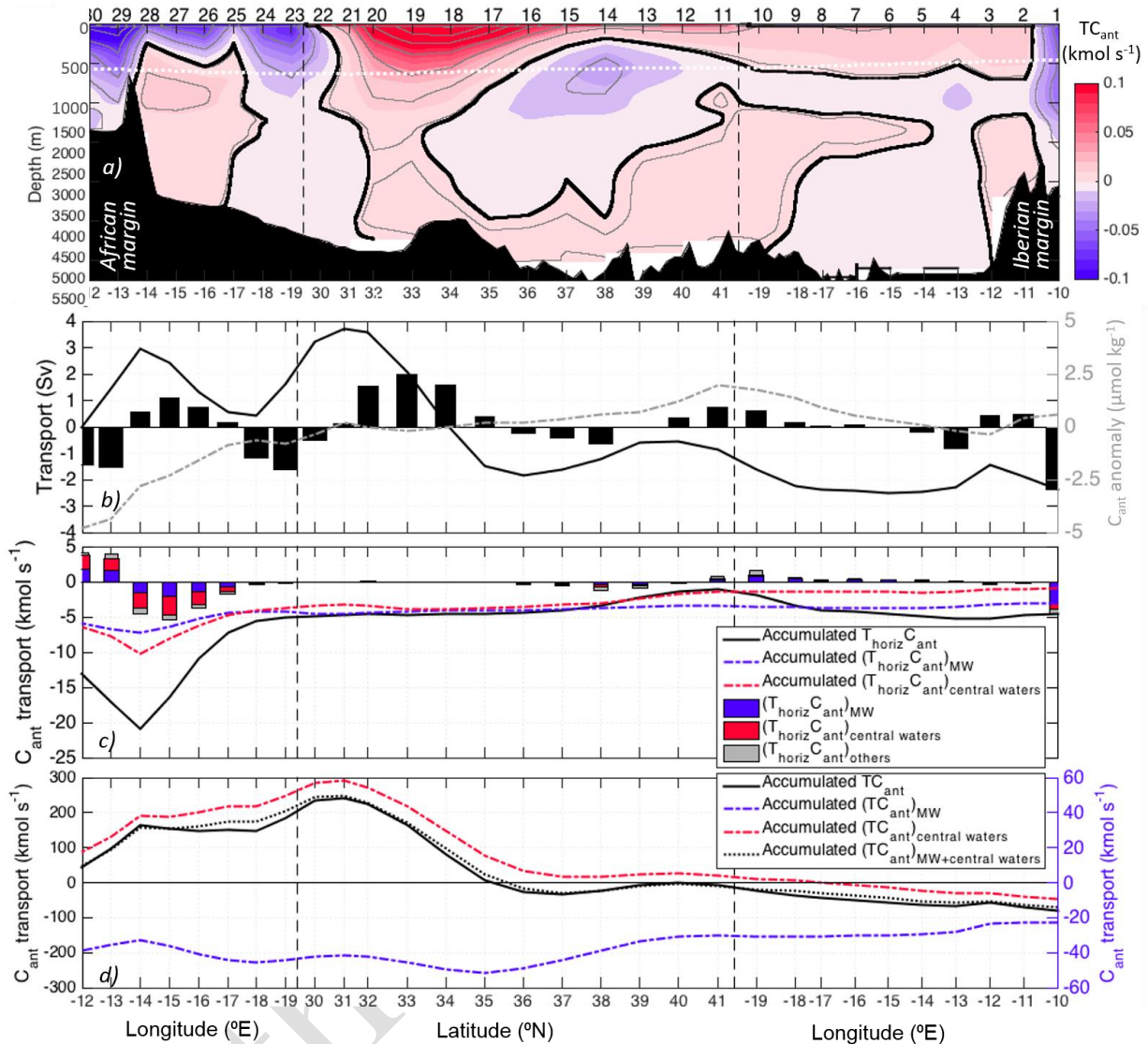
270 **Table 1.** Spatial limits, defining main surface and subsurface currents (as in Carracedo et al., 2014,  
 271 but here with depth instead of pressure as vertical coordinate, assuming that  $1\text{dbar} \sim 1\text{m}$ ); and their  
 272 corresponding volume ( $S_v$ , Sverdrup [ $= 10^6 \text{ m}^3 \text{ s}^{-1}$ ]) and  $C_{ant}$  ( $\text{kmol s}^{-1}$ ) transports. PC, Portugal  
 273 Current; IPC, Iberian Poleward Current; ACC, Azores Counter Current; AC, Azores Current; CC,  
 274 Canary Current.  $T_{sw}$  refers to sea water volume transport ( $S_v$ ).

275

	Spatial limits				Mean properties			$C_{ant}$ transport	
	St. pairs	Horiz. limits	Vert. limits, m	Condition	$\theta$ °C	$S$ psu	$C_{ant}$ $\mu\text{mol kg}^{-1}$	$TC_{ant}$ , $\text{kmol s}^{-1}$ (Net vol, $S_v$ )	
<i>Currents</i>	PC	1 to 11	9.1 to 20°W	0-800	$T_{sw} > 0$	12.0	35.68	48.7	$75 \pm 19$ ( $1.4 \pm 0.4$ )
	IPC	1 to 2	9.1 to 10.4°W	0-300	$T_{sw} < 0$ & $S \geq 35.8$	14.2	35.84	53.1	$-11 \pm 3$ ( $-0.98 \pm 0.3$ )
	ACC	12 to 18	34 to 40°N	400-1800	$T_{sw} < 0$	8.4	35.55	30.3	$-79 \pm 36$ ( $-2.5 \pm 0.8$ )
	AC	15 to 22	30 to 37°N	0-1600	$T_{sw} > 0$	11.7	35.79	39.1	$314 \pm 88$ ( $6.5 \pm 0.8$ )

276 Moving on to the  $C_{ant}$  transport decomposition shown in Eq. (3), the horizontal component  
277 ( $T_{horiz}C_{ant}$ ) has a net value of  $-13 \pm 2 \text{ kmol s}^{-1}$ , which represents a 11% contribution to the net  $C_{ant}$   
278 transport across the limits of WOA09-Box. The origin of its negative sign differs latitudinally.  
279 North of  $36^\circ\text{N}$  (north of the Azores Current), the negative sign of the horizontal component comes  
280 from the combination of positive  $C_{ant}$  anomalies (water masses with higher  $C_{ant}$  content than the  
281 mean) and a negative net transport, while south of that latitude, the negative sign comes from the  
282 combination of negative  $C_{ant}$  anomalies (water masses with lower  $C_{ant}$  content than the mean) and  
283 a positive net transport (Fig. 3b). To locate the main region contributing to  $T_{horiz}C_{ant}$ , the latter was  
284 vertically integrated and horizontally accumulated from the Iberian coast to the African coast (Fig.  
285 3c, black line). Similarly, to locate the depth range contributing the most to  $T_{horiz}C_{ant}$ , this  
286 component of the  $C_{ant}$  transport was horizontally integrated and vertically accumulated from  
287 surface to bottom (Fig. 4a, dark grey line). The strongest  $T_{horiz}C_{ant}$  occurs off the Iberian coast and  
288 across the southern section, and mostly between 650 and 1500 m. This means the horizontal  $C_{ant}$   
289 transport is driven by the combination of the intermediate circulation and the contrasting  $C_{ant}$   
290 content of the water masses at those regions.

291 To evaluate the role of the central waters and MW on the advection of  $C_{ant}$ , we isolated the  
292  $C_{ant}$  transport by water masses, as explained in section 2.2. (Eq. 3). Central waters import  $C_{ant}$  into  
293 the WOA09-Box from the North Atlantic Ocean at a net rate of  $89 \pm 55 \text{ kmol s}^{-1}$  ( $0.03 \pm 0.02 \text{ Pg-}$   
294  $\text{C yr}^{-1}$ ) (Fig. 3d, red line); whereas MW exports  $C_{ant}$  from the region of study to the North Atlantic  
295 at a net rate of  $-39 \pm 9 \text{ kmol s}^{-1}$  ( $-0.015 \pm 0.003 \text{ Pg-C yr}^{-1}$ ) (Fig. 3d, blue line), most of it northwards  
296 ( $-31 \pm 11 \text{ kmol s}^{-1}$ ; Fig. 3d, red line). These  $C_{ant}$  transports are significantly smaller than those  
297 obtained by Álvarez et al. (2005) ( $-88 \pm 8 \text{ kmol s}^{-1}$  or  $0.03 \pm 0.003 \text{ Pg-C yr}^{-1}$  for MW;  $144 \pm 8$   
298  $\text{kmol s}^{-1}$  or  $0.055 \pm 0.003 \text{ Pg-C yr}^{-1}$  for central waters). Focusing just on the horizontal component  
299 of the  $C_{ant}$  transport ( $T_{horiz}C_{ant}$ , Eq. 2) by water masses, we find 49% of this component is driven  
300 by central waters (Fig. 3c, red line and bars), 45% by MW (Fig. 3c, red line and bars), and the  
301 remaining 6% is due to the sum contribution of other water masses (not shown). Therefore, we can  
302 point to central waters and MW as the main contributors to the horizontal component of the  $C_{ant}$   
303 transport.



304  
 305 **Figure 3.** *a)*  $C_{ant}$  transports ( $\text{kmol s}^{-1}$ ) orthogonal to the WOA-Box. Grey contours represent mass  
 306 mass transport (in Sv) (black bold line is the null transport isoline). Positive (negative) values indicate  
 307  $C_{ant}$  transports into (out of) the WOA09-Box. The white dotted line corresponds to the isopycnal  
 308  $\sigma_1 = 31.65 \text{ kg m}^{-3}$  (potential density referred to 1000 dbar), which separates the upper and lower  
 309 limbs of the overturning circulation (Carracedo et al., 2014); *b)* On the left axis: the solid line is  
 310 the horizontally accumulated (from the Iberian Peninsula to Africa) volume transport (vertically  
 311 integrated for the whole water column) and the vertical bars indicate the total transport per station  
 312 pair. On the right axis: the dash-dotted grey line shows the mean value of  $C_{ant}$  anomalies ( $C_{ant}(x,$   
 313  $z) - \langle C_{ant} \rangle$ , where  $\langle C_{ant} \rangle$  represents the section mean), in  $\mu\text{mol kg}^{-1}$ , vertically averaged along the  
 314 section; *c)* Horizontally accumulated (from the Iberian Peninsula to Africa) horizontal component  
 315 of the  $C_{ant}$  transport (vertically integration for the whole water column) (black line). Mediterranean  
 316 Water horizontal  $C_{ant}$  transport (blue dash-dotted line), and central waters horizontal  $C_{ant}$  transport  
 317 (red dash-dotted line), accumulated from the Iberian to the African coast, are also shown. Vertical  
 318 bars indicate the net horizontal component of the  $C_{ant}$  transport per station pair, with the  
 319 contribution of Mediterranean (blue) and Central Waters (red) specified; *d)* Horizontally

320 accumulated (from the Iberian Peninsula to Africa)  $C_{\text{ant}}$  transport (vertically integrated for the  
 321 whole water column, black line). Mediterranean Water  $C_{\text{ant}}$  transport (blue dash-dotted line, right  
 322 axis), central waters  $C_{\text{ant}}$  transport (red dash-dotted line, left axis), and the sum of  $C_{\text{ant}}$  transports  
 323 of both water masses (dotted line, left axis), all accumulated from the Iberian peninsula to Africa,  
 324 are also shown.

### 325 3.3 Anthropogenic $\text{CO}_2$ inventory and role of the overturning circulation

326 For the WOA09-Box enclosed region, the  $C_{\text{ant}}$  inventory was computed by vertical  
 327 integration of the  $C_{\text{ant}}$  grid data (Eq. 4). We estimated a total inventory of  $1.18 \pm 0.20$  Pg-C, which,  
 328 considering the total surface area of WOA09-Box ( $1.36 \times 10^{12}$  m<sup>2</sup>), results in a specific inventory  
 329 of  $72 \pm 12$  molC m<sup>-2</sup>. Lee et al. (2003), based on *in situ* data (1990-1998 period), provided an  
 330 estimate, referenced to 1994, of  $66.2$  molC m<sup>-2</sup> for the 30°N–40°N latitudinal band. Similarly, and  
 331 also based on hydrographic cruise data (1993–2003 period), Vázquez-Rodríguez et al. (2009a)  
 332 provided a specific  $C_{\text{ant}}$  inventory of around  $75$  molC m<sup>-2</sup> (referenced to 1994) at 30°N. When  
 333 rescaled to year 2000 (reference year in this study) (Eq. A1), both values ( $73.2$  and  $82.9$  molC m<sup>-2</sup>,  
 334 respectively) are comparable to our estimate within the uncertainty. At more regional scale, Flecha  
 335 et al. (2012) determined a specific  $C_{\text{ant}}$  inventory of  $33.5 \pm 3.2$  molC m<sup>-2</sup> in the Gulf of Cadiz (Fig.  
 336 1, total area of  $0.04 \times 10^{12}$  m<sup>2</sup>) from *in situ* cruise data (October 2008). The GLODAPv2-based  
 337 estimate for that particular region is  $40 \pm 8$  molC m<sup>-2</sup> (referenced to 2000). To compare both  
 338 estimates, we rescaled Flecha's et al. (2012) value to year 2000 (Eq. A1), resulting in  $29.3 \pm 2.8$   
 339 molC m<sup>-2</sup>. Although our estimate is slightly larger than that of Flecha's et al. (2012), they are not  
 340 statistically different. Note the specific  $C_{\text{ant}}$  inventory in the Gulf of Cadiz region is smaller in  
 341 comparison to the average for the entire WOA09-Box region (see Fig. B3 in Appendix B). That  
 342 could be interpreted as the Gulf of Cadiz, despite being the location where the exchange of  $C_{\text{ant}}$   
 343 between central and intermediate water masses takes place, is not the region where  $C_{\text{ant}}$  is stored.  
 344 Finally, by multiplying the  $C_{\text{ant}}$  inventory by  $k_t$  ( $0.0169$  yr<sup>-1</sup>), we obtained a  $C_{\text{ant}}$  storage rate of  
 345  **$0.020 \pm 0.003$  Pg-C yr<sup>-1</sup>** (that is,  **$53 \pm 9$  kmol s<sup>-1</sup>**). That implies a specific  $C_{\text{ant}}$  storage rate of  $1.22$   
 346  $\pm 0.21$  molC m<sup>-2</sup> y<sup>-1</sup>. Ríos et al. (2001), who used a set of 12 cruises carried out in the North-East  
 347 Atlantic between 1977 and 1997, estimated a similar but slightly lower specific storage rate of  $0.95$   
 348 molC m<sup>-2</sup> y<sup>-1</sup>. The good overall agreement with *in situ*-based studies in terms of  $C_{\text{ant}}$   
 349 inventory/storage rate adds confidence to our climatology-based estimates.

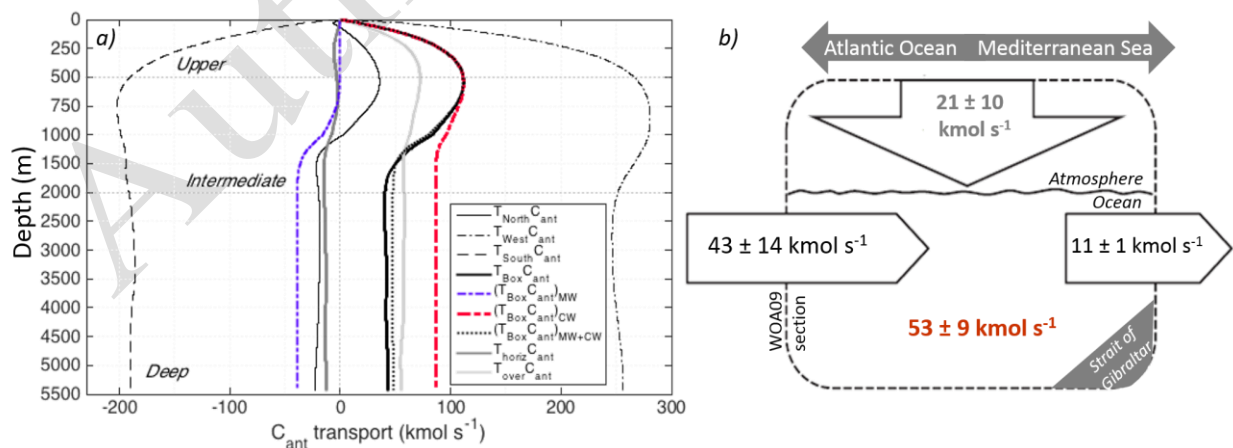
350  
 351 According to the transport decomposition (Eq. 2), there is a net overturning component,  
 352  $T_{\text{over}}C_{\text{ant}}$ , of  $56 \pm 2$  kmol s<sup>-1</sup>. Note the barotropic component ( $T_{\text{baro}}C_{\text{ant}} = 0.2 \pm 8$  kmol s<sup>-1</sup>, Eq. 2) has  
 353 an almost negligible contribution to the net  $C_{\text{ant}}$  flux, so we are just discussing horizontal vs.  
 354 overturning components. By vertical (surface-to-bottom) accumulation of  $T_{\text{over}}C_{\text{ant}}$  (Fig. 4a, light  
 355 grey line), we see that the upper limb of the overturning circulation ( $\sigma_1 < 31.65$  kg m<sup>-3</sup>, Fig. 3a,  
 356 broadly upper 500 m) is the main driver of the term. That is, the  $C_{\text{ant}}$ -loaded surface waters (Fig.  
 357 2) imported by the upper overturning cell ( $72 \pm 6$  kmol s<sup>-1</sup>) will not be compensated for the less  
 358  $C_{\text{ant}}$ -loaded waters (Fig. 2) exported by the lower limb ( $-17 \pm 9$  kmol s<sup>-1</sup>), thus resulting in a positive  
 359  $T_{\text{over}}C_{\text{ant}}$  component ( $56 \pm 2$  kmol s<sup>-1</sup>). This component is four times larger than the horizontal  
 360 component ( $T_{\text{horiz}}C_{\text{ant}}$ ,  $-13 \pm 2$  kmol s<sup>-1</sup>), meaning that net  $C_{\text{ant}}$  transport is mostly driven by  
 361 overturning circulation (80%) rather than by horizontal circulation (20%). This resembles the  
 362 larger scale, where the North Atlantic meridional overturning circulation is found to drive both the  
 363 magnitude and variability of the  $C_{\text{ant}}$  transport across the Subpolar North Atlantic (Zunino et al.,



364 2014). Our results confirm the cruise-based findings of Alvarez et al. (2005), and let us further  
 365 denote this physical mechanism as the main driver of the net  $C_{ant}$  transport in the North-East  
 366 Atlantic in the long-term average context of an annual climatology.

367  
 368 As for the overturning circulation within the box, when MW is formed in the Gulf of Cadiz  
 369 (with an upper bounded MW production rate of 2 Sv, Carracedo et al. 2014, 2015),  $1.2 \pm 0.2$  Sv  
 370 of central waters are entrained into the sinking plume of Mediterranean Outflow Water (Carracedo  
 371 et al., 2014; Barbosa Aguiar et al., 2015). Since central waters at this location have a  $C_{ant}$   
 372 concentration of about  $60 \pm 6 \mu\text{mol kg}^{-1}$  (Huertas et al., 2009), this entrainment provides about  $74$   
 373  $\pm 14 \text{ kmol s}^{-1}$  of  $C_{ant}$  ( $0.03 \pm 0.01 \text{ Pg-C yr}^{-1}$ ) to intermediate layers. Prior studies have reported  
 374 higher amounts of  $C_{ant}$  drawdown to depth by central waters ( $185 \text{ kmol s}^{-1}$  or  $0.07 \text{ Pg-C yr}^{-1}$ , Ríos  
 375 et al. 2001;  $151 \pm 14 \text{ kmol s}^{-1}$  or  $0.06 \pm 0.01 \text{ Pg-C yr}^{-1}$ , Álvarez et al. 2005). Those studies, however,  
 376 could have overestimated the volume of central waters (3-4 Sv) being entrained, as shown in the  
 377 recent study by Barbosa Aguiar et al. (2015). Half of those  $74 \pm 14 \text{ kmol s}^{-1}$ ,  $37 \pm 7 \text{ kmol s}^{-1}$  ( $0.6$   
 378  $\pm 0.1$  Sv, Carracedo et al. 2014), are finally merged with  $0.78 \pm 0.05$  Sv (Soto-Navarro et al.,  
 379 2010) of Mediterranean Outflow Water to form MW. Considering a mean  $C_{ant}$  concentration of  $52$   
 380  $\pm 6 \mu\text{mol kg}^{-1}$  for the Mediterranean Outflow Water (Huertas et al., 2009), this overflow provides  
 381 an input of  $42 \pm 5 \text{ kmol s}^{-1}$  of  $C_{ant}$ . Therefore, the resulting MW is going to contribute with around  
 382  $79 \pm 9 \text{ kmol s}^{-1}$  of  $C_{ant}$ . According to our results,  $39 \pm 9 \text{ kmol s}^{-1}$  of  $C_{ant}$  are (net) exported by MW  
 383 out of the WOA09-Box, so that the remaining  $40 \pm 13 \text{ kmol s}^{-1}$  ( $0.015 \pm 0.005 \text{ Pg-C yr}^{-1}$ ) would  
 384 be available to contribute to the total  $C_{ant}$  storage rate within the box ( $0.020 \pm 0.003 \text{ Pg-C yr}^{-1}$ ).  
 385

386 In the context of the subtropical North Atlantic (total area of  $16.6 \times 10^{12} \text{ m}^2$ ), the singular  
 387 overturning cell that occupies the localized region of the Gulf of Cadiz can be pointed as a relevant  
 388 conduit through which  $C_{ant}$  sinks ( $0.03 \text{ Pg-C yr}^{-1}$ ) and ultimately contributes to the storage rate at  
 389 intermediate layers ( $0.015 \pm 0.005 \text{ Pg-C yr}^{-1}$ ) within the WOA09-Box. This contribution of the  
 390 newly formed MW to the storage rate represents a 6% of the total  $C_{ant}$  stored in the subtropical  
 391 North Atlantic ( $0.280 \pm 0.011 \text{ Pg-C yr}^{-1}$  referenced to 2004, Pérez et al., 2013;  $0.262 \pm 0.010 \text{ Pg-}$   
 392  $\text{C yr}^{-1}$  referenced to 2000, Eq. A1), despite the Gulf of Cadiz accounting for less than 1% of the  
 393 subtropical North Atlantic surface.  
 394



395  
 396 **Figure 4.** a) Vertical distribution of vertically (surface-to-bottom) accumulated  $C_{ant}$  transports  
 397 ( $T_{North}C_{ant}$ ,  $T_{West}C_{ant}$ ,  $T_{South}C_{ant}$ , refer to the  $C_{ant}$  transports across north, west and south sections,  
 398 respectively;  $T_{Box}C_{ant}$ , the  $C_{ant}$  transport across the whole section;  $(T_{Box}C_{ant})_{MW}$ ,  $(T_{Box}C_{ant})_{CW}$  and

399  $(T_{Box}C_{ant})_{MW+CW}$  refers to the  $C_{ant}$  transport by the Mediterranean Water, by central waters, and by  
 400 the sum of those two water masses, respectively; and  $T_{horiz}C_{ant}$  and  $T_{over}C_{ant}$  the horizontal and  
 401 overturning components, transports in  $\text{kmol s}^{-1}$ ; c) Simplified  $C_{ant}$  budget scheme for WOA09-  
 402 Box.

403 Finally, closing the  $C_{ant}$  budget in the North-East Atlantic at climatological scale (Fig. 4b),  
 404 we estimated the anthropogenic air-to-sea contribution for WOA-Box following Eq. (6). The net  
 405 annual  $F_{Air-sea}C_{ant}$  was  $21 \pm 10 \text{ kmol s}^{-1}$ , not distinguishable, within the uncertainty, to the value  
 406 obtained by Álvarez et al. (2005) of  $13 \text{ kmol s}^{-1}$ . The magnitude of this term ( $21 \pm 10 \text{ kmol s}^{-1}$ )  
 407 represents 40% of the total  $C_{ant}$  storage ( $53 \pm 9 \text{ kmol s}^{-1}$ ), while advection ( $T_{Box}C_{ant} + T_{Strait}C_{ant} =$   
 408  $32 \pm 14 \text{ kmol s}^{-1}$ ) contributes the remaining 60% to the  $C_{ant}$  budget (11% due to the horizontal  
 409 component and 48% to the overturning component).  $C_{ant}$  advection being predominant over air-  
 410 sea  $C_{ant}$  flux is a result in agreement with Álvarez et al. (2005). They concluded that 17% of the  
 411  $C_{ant}$  storage was attributable to uptake from the atmosphere, compared to 83% coming from the  
 412 ocean circulation. Ríos et al. (2001), however, had previously estimated that the atmospheric input  
 413 of  $C_{ant}$  ( $0.47 \text{ mol m}^{-2} \text{ yr}^{-1}$ ) contributed as much as advection to the  $C_{ant}$  inventory within the Iberian  
 414 Basin (at  $20^{\circ}\text{W}$  and  $37\text{-}47^{\circ}\text{N}$  latitudinal range).

415 The total (natural and anthropogenic)  $\text{CO}_2$  air-sea flux in the region,  $F_{Air-sea} \text{CO}_2$  (section  
 416 2.4.), has a magnitude of  $27 \pm 8 \text{ kmol s}^{-1}$  (annual average of monthly estimates), meaning that on  
 417 annual timescales the North-East Atlantic acts as a sink for atmospheric  $\text{CO}_2$ . The anthropogenic  
 418 portion of the total  $F_{Air-sea} \text{CO}_2$ , inferred from our results at the  $28\text{-}42^{\circ}\text{N}$  latitudinal range ( $21 \pm 10$   
 419  $\text{kmol s}^{-1}$ ), represents more than three quarters of the total  $\text{CO}_2$  uptake ( $78 \pm 30\%$ ). The difference  
 420 between both magnitudes,  $F_{Air-sea} \text{CO}_2$  and  $F_{Air-sea}C_{ant}$ , is attributable to the natural component ( $F_{Air-}$   
 421  $seaC_{nat}$ ,  $6 \pm 12 \text{ kmol s}^{-1}$ ). In the North Atlantic, the air-sea  $\text{CO}_2$  fluxes result from anthropogenic  
 422 forcing and progressive northward cooling of the upper limb of the meridional overturning  
 423 circulation (Pérez et al., 2013), the latter being ultimately responsible for the North Atlantic uptake  
 424 of natural  $\text{CO}_2$  (Pérez et al., 2013). For a box encompassing the subtropical region (between  $25^{\circ}\text{N}$   
 425 and the A25 section, see their Fig. 1a), Pérez et al. (2013) found the anthropogenic air-sea  $\text{CO}_2$   
 426 uptake dominated ( $60 \pm 25\%$  of the total air-sea  $\text{CO}_2$  flux) over the natural component; whereas  
 427 for the subpolar region (between the A25 section and the Nordic sills, see their Fig. 1a), the natural  
 428 component was largely prevalent over the anthropogenic one (which only represented  $18 \pm 13\%$   
 429 of the total air-sea  $\text{CO}_2$  flux). The anthropogenic air-sea  $\text{CO}_2$  uptake inferred from our estimates  
 430 within the domain of the WOA09-Box ( $29.5\text{-}41.5^{\circ}\text{N}$  latitudinal range) leads us to interpret the  
 431 region of study as part of the air-sea  $C_{ant}$ -dominated subtropical regime, as defined by Pérez et al.  
 432 (2013). However, because of the large uncertainties accompanying the air-sea fluxes and the  
 433 indirect nature of the  $F_{Air-sea}C_{ant}$  estimate, our interpretation about  $C_{nat}$  v.s.  $C_{ant}$  contribution must  
 434 be taken with some caution.

#### 435 **4 Summary and concluding remarks**

436 In this study, we presented a description of the mean annual  $C_{ant}$  transport in the Azores-  
 437 Gibraltar region and evaluated the role of the horizontal and overturning circulation in terms of  
 438  $C_{ant}$  storage in the North-East Atlantic. To the best of our knowledge,  $C_{ant}$  budget estimates are

439 given for the first time in this region by combination of  $C_{\text{ant}}$  GLODAPv2-derived concentrations  
440 and WOA09-derived absolute velocity field.

441 We obtained a net  $C_{\text{ant}}$  transport across the WOA09-Box section of  $43 \pm 14 \text{ kmol s}^{-1}$ . The  
442 0-1500 m depth range encompasses more than 90% of the  $C_{\text{ant}}$  advection, underlining the  
443 upper/intermediate circulation as responsible for  $C_{\text{ant}}$  distribution and recirculation within the  
444 region. Azores and Portugal Currents account for the greatest  $C_{\text{ant}}$  inflow, with  $389 \pm 90 \text{ kmol s}^{-1}$ .  
445 Most of it recirculates southwards in the Canary Current ( $-214 \pm 34 \text{ kmol s}^{-1}$  of  $C_{\text{ant}}$ ), which  
446 provides the main advective  $C_{\text{ant}}$  export path across the limits of WOA09-Box. At intermediate  
447 levels, we find the secondary  $C_{\text{ant}}$  export route to be the Azores Counter Current, with a westwards  
448  $C_{\text{ant}}$  flux of  $-79 \pm 36 \text{ kmol s}^{-1}$ .

449 At annual mean climatological scale, we estimated a total  $C_{\text{ant}}$  inventory of  $1.18 \pm 0.20 \text{ Pg-}$   
450  $\text{C}$  (specific inventory of  $72 \pm 12 \text{ mol C m}^{-2}$ ) and a  $C_{\text{ant}}$  storage rate of  $0.020 \pm 0.003 \text{ Pg-C yr}^{-1}$  ( $53$   
451  $\pm 9 \text{ kmol s}^{-1}$ ). The advection of  $C_{\text{ant}}$  contributes to 60% of the North-East Atlantic  $C_{\text{ant}}$  storage  
452 rate. Of the 60% contribution, 11% is driven by horizontal circulation ( $-13 \pm 2 \text{ kmol-C}_{\text{ant}} \text{ s}^{-1}$ ) and  
453 48% is driven by overturning circulation ( $56 \pm 2 \text{ kmol-C}_{\text{ant}} \text{ s}^{-1}$ ). Overturning circulation is,  
454 therefore, the physical mechanism dominating the  $C_{\text{ant}}$  transport across the limits of WOA09-Box  
455 and, ultimately, the  $C_{\text{ant}}$  storage rate in the North-East Atlantic. The remaining 40% ( $21 \pm 10 \text{ kmol}$   
456  $\text{s}^{-1}$ ) is due to the atmospheric  $C_{\text{ant}}$  being taken up by the ocean. The anthropogenic fraction of the  
457 atmospheric  $\text{CO}_2$  accounts for more than three quarters ( $78 \pm 30\%$ ) of the total annual air-sea  
458 (natural and anthropogenic)  $\text{CO}_2$  uptake at a climatological scale in the region ( $27 \pm 8 \text{ kmol s}^{-1}$ ).

459 Exploring the water mass transformation as result of the overturning cell within the box,  
460 we found that the downward export of  $C_{\text{ant}}$ -loaded central waters in the Gulf of Cadiz, and  
461 subsequent formation of MW (between 800 to 1200 dbar) lets  $74 \pm 14 \text{ kmol s}^{-1}$  of  $C_{\text{ant}}$  be  
462 drawdown from upper to intermediate ocean. In particular, the entrainment of central waters ( $37$   
463  $\pm 7 \text{ kmol s}^{-1}$  of  $C_{\text{ant}}$ ) to feed Mediterranean Outflow Water ( $42 \pm 5 \text{ kmol s}^{-1}$  of  $C_{\text{ant}}$ ), provides the  
464 resulting MW with  $79 \pm 9 \text{ kmol s}^{-1}$  of  $C_{\text{ant}}$ . Of that amount,  $39 \pm 9 \text{ kmol s}^{-1}$  (net  $C_{\text{ant}}$  transport by  
465 MW across the limits of WOA09-Box) will be ultimately advected into the North Atlantic, while  
466 the remaining  $40 \pm 15 \text{ kmol s}^{-1}$  will be available to contribute to the total  $C_{\text{ant}}$  storage rate within  
467 the Azores-Gibraltar Strait region.

468 Within the context of the entire North Atlantic, the Gulf of Cadiz represents much less than  
469 1% of the total area, yet annually (climatological mean) the newly formed MW accounts for a  $C_{\text{ant}}$   
470 storage rate in the North-East Atlantic of  $0.020 \pm 0.003 \text{ Pg-C yr}^{-1}$ , which represents 6% of the  $C_{\text{ant}}$   
471 storage rate in the entire subtropical North Atlantic ( $0.280 \pm 0.011 \text{ Pg-C yr}^{-1}$ , referenced to 2004;  
472 Pérez et al., 2013). Our results have let us firmly point to this singular region as a long-term  $C_{\text{ant}}$   
473 sink and deep storage basin in a year-round basis. Regional estimates of the  $C_{\text{ant}}$  inventory in key  
474 regions such as the North-East Atlantic are, therefore, a significant contribution towards the  
475 refinement of the global deep  $\text{CO}_2$  storage estimates.

476 While  $C_{\text{ant}}$  transports could be biased towards lower-bound estimates, due to the smoothed  
477 nature of the density field from which geostrophic velocities are derived,  $C_{\text{ant}}$  inventory/storage  
478 rate estimates have been proved to be in good agreement with previous cruise-data-based values.

479 Overall, we aim to highlight the suitability of the joint use of the GLODAPv2 and WOA09  
480 databases to depict the annual mean state of the  $C_{\text{ant}}$  budget in the ocean.

## 481 Acknowledgments and Data

482 This work was funded by the Spanish National Research Council (CSIC), through the EU  
483 H2020 project AtlantOS (“Optimizing and Enhancing the Integrated Atlantic Ocean Observing  
484 Systems Research”, RIA), financed by the European Commission’s H2020 Framework  
485 Programme under grant agreement no. 633211. The first author is being funded by the University  
486 of Vigo, through the Galician I2C Plan for postdoctoral research. F.F. Pérez and G. Rosón were  
487 supported by the Spanish Ministry of Economy through the CATARINA (CTM2010-17141) and  
488 BOCATS (CTM2013-41048-P) projects, both co-funded by the Fondo Europeo de Desarrollo  
489 Regional (FEDER). We thank S. Torres-Valdés for the constructive feedback provided and to E.  
490 D. Barton for the English proofreading. Likewise, we gratefully acknowledge the data sources for  
491 this study: potential temperature and salinity to derive geostrophic velocity estimates, from the  
492 2009 World Ocean Atlas (WOA09) database (Boyer et al., 2009)  
493 (<http://www.nodc.noaa.gov/OC5/WOA09/>), carbonate system variables to estimate  $C_{\text{ant}}$ , from the  
494 GLODAPv2 database (<http://cdiac.ornl.gov/oceans/GLODAPv2/>), and the  $p\text{CO}_2$  climatology of  
495 Takahashi et al. (2009) ([www.ldeo.columbia.edu](http://www.ldeo.columbia.edu)).

## 496 Appendix A. Supplementary Text

### 497 A.1. The $\phi C_T^0$ method for $C_{\text{ant}}$ estimate

498 The anthropogenic  $\text{CO}_2$  in the ocean ( $C_{\text{ant}}$ ) is not a tracer that can be directly measured, as both  
499 natural and anthropogenic  $\text{CO}_2$  molecules are identical although they present different isotopic ( $\delta^{13}\text{C}/\delta^{12}\text{C}$ )  
500 ratios (Quay et al., 2007). Moreover, the anthropogenic signal is less than 1% of the oceanic  $\text{CO}_2$   
501 load (up to 3.5% in surface layers), thus adding difficulty to its study and accurate quantification.  
502 In the late 1970s, authors such as Brewer (1978) or Chen and Millero (1979) introduced for the  
503 first time the so-called back-calculation techniques, an indirect  $C_{\text{ant}}$  estimate based on direct  
504 measurements of total inorganic carbon ( $C_T$ ), total alkalinity ( $A_T$ ) and dissolved oxygen.  $C_{\text{ant}}$  is  
505 referred to as the difference between the preformed total inorganic carbon ( $C_T^0$ , note hereafter  
506 superscript 0 will mean preformed) and its concentration after the preindustrial era ( $C_T^{0\pi}$ ).  $C_T^0$  is  
507 determined as  $C_T^0 = C_T - \Delta C_{\text{bio}}$ , where  $\Delta C_{\text{bio}}$  stands for the organic matter  
508 oxidation/remineralization processes and the dissolution of  $\text{CaCO}_3$ ; while  $C_T^{0\pi}$  is determined as  
509  $C_T^{0\pi} = C_T^{\text{eq},\pi} + \Delta C_{\text{dis}}^{\pi}$ , where  $C_T^{\text{eq},\pi}$  is the total inorganic carbon in atmosphere-ocean equilibrium  
510 in the preindustrial era, and  $\Delta C_{\text{dis}}^{\pi}$  is the disequilibrium in the atmosphere-ocean interphase.

511 From the early approaches, back-calculation techniques were subject to various  
512 improvements, one of the most recent being the so-called  $\phi C_T^0$  method (Vázquez-Rodríguez et al.,  
513 2009b, see their Eq.10). The  $\phi C_T^0$  method was developed under the assumption that  
514 biogeochemical processes that modulate oceanic  $C_T$  have operated invariably with time. The  
515 method, which shares principles with the more classical  $\Delta C^*$  method of Gruber et al. (1996),  
516 proposes different parameterizations to calculate  $\Delta C_{\text{dis}}$  and the preformed alkalinity ( $A_T^0$ ) to assess  
517 the contribution of  $\text{CaCO}_3$  dissolution to  $C_T$ .  $A_T^0$  is based on the concept of potential alkalinity  
518  $\text{PA}_T$  and is defined as  $A_T^0 = \text{PA}_T - (\text{NO}_3^0 + \text{PO}_4^0)$  (Vázquez-Rodríguez et al., 2012), where  $\text{NO}_3^0$   
519 and  $\text{PO}_4^0$  are determined as  $\text{NO}_3^0 = \text{NO}_3 - \text{AOU}/R_{\text{ON}}$  and  $\text{PO}_4^0 = \text{PO}_4 - \text{AOU}/R_{\text{OP}}$ . AOU stands



520 for Apparent Oxygen Utilisation, that is, the difference between the saturated concentrations of  
 521 oxygen (Benson and Krause, 1984) and the measured concentrations of oxygen; and  $R_{ON}$  and  $R_{OP}$   
 522 are the Redfield ratios proposed by Anderson and Sarmiento (1994), satisfactorily applied in the  
 523 North Atlantic for the estimate of  $C_{ant}$  by, e.g., Pérez et al. (2008; 2010; 2013) or Ríos et al. (2012,  
 524 2015). A relevant aspect of the  $\phi_{CT^0}$  method parameterizations is that they are not CFC-reliant  
 525 (i.e., there is no need of arbitrary references for  $C_{ant=0}$  based on CFCs measurements). Instead, the  
 526  $\phi_{CT^0}$  method uses conservative properties of the subsurface layer (100–200 m) from the whole  
 527 Atlantic to build these parametrizations. In their study, Vázquez-Rodríguez et al. (2009a) used 10  
 528 WOCE cruises along the Atlantic spanning between 1993 and 2003, for which CFC-11 and CFC-  
 529 12 measurements were available, to apply a shortcut method (Thomas and Ittekkot, 2001) for the  
 530 estimate of  $C_{ant}$  in waters  $\theta > 5^\circ\text{C}$ . Since the average age of the water masses in the Atlantic 100–  
 531 200m depth domain is under 25 years, the use of a shortcut method is considered to be appropriate  
 532 (Matear et al., 2003). With the shortcut-based  $C_{ant}$  estimates, and the additional measurements of  
 533 temperature, salinity,  $C_T$ ,  $A_T$ , and AOU,  $\Delta C_{dis}$  is parametrized by means of multilinear  
 534 regressions. Once parametrized,  $\Delta C_{dis}$  can therefore be estimated without further need of CFC  
 535 data. For waters  $\theta < 5^\circ\text{C}$ , the MLR parametrization is substituted by an Optimum Multiparameter  
 536 Analysis (Vázquez et al., 2009a). This procedure lets the improvement of  $C_{ant}$  estimations in cold  
 537 deep waters where complex-mixing processes between northern and southern hemispheric source  
 538 water masses takes place. The overall uncertainty of the  $\phi_{CT^0}$  method is  $\pm 5.2 \mu\text{mol kg}^{-1}$ , as  
 539 computed by Vázquez-Rodríguez et al. (2009b) by random propagation of the errors associated  
 540 with the input variables necessary to apply the method. This value was used in this study to perform  
 541 a perturbation analysis of uncertainties (see Appendix A3).

542 Several intercomparison studies in the Atlantic Ocean support the robustness and validity  
 543 of the  $\phi_{CT^0}$  method (Ríos et al., 2001, 2010; Álvarez et al., 2005; Pérez et al., 2010; Fajar et al.,  
 544 2012; Flecha et al., 2012). Further details of the method can be found in Vázquez-Rodríguez et al.  
 545 (2009b), and the Matlab® code is freely available on the IIM-CSIC CO<sub>2</sub> Group webpage  
 546 (<http://ocean0.iim.csic.es/co2group/index.html>).

547 In the current study, we applied the  $\phi_{CT^0}$  back-calculation technique to GLODAPv2 bottle  
 548 data ([http://cdiac.ornl.gov/ftp/oceans/GLODAPv2/Data\\_Products/data\\_product/](http://cdiac.ornl.gov/ftp/oceans/GLODAPv2/Data_Products/data_product/)).  $C_{ant}$  estimates  
 549 were scaled from their original cruise year ( $C_{ant}(t_1)$ ) to year 2000 ( $C_{ant}(t_2)$ ) using the transient  
 550 steady state approach (Tanhua et al., 2006). We selected year 2000 as reference to be concordant  
 551 with the pCO<sub>2</sub> climatology of Takahashi et al. (2009) (dataset used in this study to estimate the air-  
 552 sea CO<sub>2</sub> flux, section 2.4).  $C_{ant}$  concentrations were time-normalized following:

$$553 \quad C_{ant}(t_2) = C_{ant}(t_1) (1 + k_t)^{(t_2 - t_1)} \quad (\text{A1})$$

554 where  $t_1$  corresponds to each GLODAPv2 cruise occupation year;  $t_2$  is the reference year 2000;  
 555 and  $k_t$  is the annual  $C_{ant}$  rate of increase ( $k_t = 0.0169 \pm 0.001 \text{ y}^{-1}$ , Steinfeldt et al. (2009)).  
 556 Normalizing  $C_{ant}$  estimates to a year of reference ensures a time homogeneous recordset, whereas  
 557 it just entails a minor correction, that is, it only accounts for 1.7% of the value of  $C_{ant}$  for each year

558 of difference with an error of 0.1% (Guallart et al. 2015). Note this error is two orders of magnitude  
 559 smaller than the 10% of error associated to the  $C_{\text{ant}}$  transport estimate (Appendix A.2.1).

## 560 A.2. Uncertainty estimate

### 561 A.2.1. $C_{\text{ant}}$ transport

562 Tracer transports come from the product of volume fluxes and the tracer concentration. The  
 563 error associated to any transport can be computed by applying the error propagation formula (Eq.  
 564 A2). Being  $F=f(x_1, x_2, \dots, x_N)$ , and assuming a zero-correlation between the independent variables,  
 565 the error propagation formula is:

$$566 \quad \varepsilon = \left[ \left( \frac{\partial F}{\partial x_1} \right)^2 \varepsilon_1^2 + \left( \frac{\partial F}{\partial x_2} \right)^2 \varepsilon_2^2 + \dots + \left( \frac{\partial F}{\partial x_N} \right)^2 \varepsilon_N^2 \right]^{1/2} \quad (\text{A2})$$

567 In view of that, the error of the  $C_{\text{ant}}$  transport can be computed as the sum of errors due to both the  
 568 mass transport (transport-derived uncertainty,  $\sigma_{T_{\text{Cant}}^T}$ ) and the  $C_{\text{ant}}$  concentrations ( $C_{\text{ant}}$ -derived  
 569 uncertainty,  $\sigma_{T_{\text{Cant}}^{\text{Cant}}}$ ), such as:

$$570 \quad \varepsilon = \sqrt{(\sigma_{T_{\text{Cant}}^T})^2 + (\sigma_{T_{\text{Cant}}^{\text{Cant}}})^2} \quad (\text{A3})$$

571  $\sigma_{T_{\text{Cant}}^T}$  was calculated from the covariance matrix of errors for mass transport (diagonal matrix of  
 572 covariance at the reference level for all station pairs), as obtained from the two-dimensional  
 573 geostrophic inverse ocean model (Carracedo et al., 2014). On the other hand,  $\sigma_{T_{\text{Cant}}^{\text{Cant}}}$  was  
 574 estimated as the product of the net transport across the subregion considered and the standard  
 575 deviation of the  $C_{\text{ant}}$  concentration at the same subregion.

576 To illustrate this, we show as an example the uncertainty estimate for the net  $C_{\text{ant}}$  transport  
 577 across the WOA09-Box. Following the error propagation formula (Eq. A3), this results in:

$$578 \quad \varepsilon_{T_{\text{Box}} C_{\text{ant}}} = \sqrt{[\sigma_{T_{\text{Cant}}^T}]^2 + [\text{std}(C_{\text{ant}}) \times T_{\text{Box}}]^2} =$$

$$579 \quad = \sqrt{[14.0]^2 + [0.17]^2} = 14 \text{ kmols}^{-1}$$

580 Where  $\text{std}(C_{\text{ant}})$  refers to the standard deviation of  $C_{\text{ant}}$  in the section ( $\text{std}(C_{\text{ant}})=14.8 \mu\text{mol kg}^{-1}$ ,  
 581 that is  $1.52 \times 10^{-5} \text{ kmol m}^{-3}$ , by multiplying by a reference density for seawater of  $1026 \text{ kg m}^{-3}$ ), and  
 582  $T_{\text{Box}}$  ( $0.011 \times 10^6 \text{ m}^3 \text{ s}^{-1}$ ) refers to the net volume transport across the box.

### 583 A.2.2. $C_{\text{ant}}$ storage rate

584 Vázquez Rodríguez et al. (2009a) and Pérez et al. (2013) calculated the uncertainty related  
 585 to the  $C_{\text{ant}}$  inventory estimate by randomly propagating over depth a  $5 \mu\text{mol kg}^{-1}$  standard error  
 586 for  $C_{\text{ant}}$ . They obtained values of  $\pm 1 \text{ mol-C m}^{-2}$  and  $\pm 2 \text{ mol-C m}^{-2}$  when integrated down to 3000

587 m and 6000 m, respectively. By applying that  $\pm 2 \text{ mol m}^{-2}$  uncertainty to the WOA09-Box area, we  
 588 obtained a total value of  $\pm 9 \text{ kmol s}^{-1}$ .

### 589 A.2.3. Air-sea $\text{CO}_2$ and $C_{\text{ant}}$ flux

590 The uncertainty estimate for the air-sea  $\text{CO}_2$  flux was given as the mean standard error of  
 591 the monthly  $F_{\text{Air-seaCO}_2i}$  (with  $i=1\dots 12$ ) estimate within the WOA09-Box:

$$592 \quad \varepsilon F_{\text{Air-seaCO}_2} = \frac{\text{std}(F_{\text{Air-seaCO}_2i})}{\sqrt{12}} = \frac{26.1}{\sqrt{12}} = 8 \text{ kmol s}^{-1} \quad (\text{A4})$$

593 The air-sea  $C_{\text{ant}}$  flux,  $F_{\text{Air-sea}C_{\text{ant}}}$ , is the result from equation (5), so its uncertainty was estimated by  
 594 means of error propagation (Eq. A2), such as:

$$595 \quad \varepsilon F_{\text{Air-sea}C_{\text{ant}}} = \sqrt{(\varepsilon C_{\text{ant}} \text{ storage rate})^2 + (\varepsilon T_{\text{Strait}} C_{\text{ant}})^2 + (\varepsilon_G T_{\text{Box}} C_{\text{ant}})^2}$$

$$596 \quad = \sqrt{(9)^2 + (1)^2 + (5)^2} = 6 \text{ kmols}^{-1} \quad (\text{A5})$$

597  $\varepsilon C_{\text{ant}}$  storage rate is the value obtained in section A.2.2;  $\varepsilon T_{\text{Strait}} C_{\text{ant}}$  is the value estimated by  
 598 (Huertas et al., 2009); and, finally,  $\varepsilon_G T_{\text{Box}} C_{\text{ant}}$  corresponds to the uncertainty estimate of the net  
 599  $C_{\text{ant}}$  transport for the WOA09-Box. With the particular purpose of providing a tighter final  
 600 uncertainty to the  $F_{\text{Air-sea}C_{\text{ant}}}$  estimate, we recalculated a new uncertainty for the  $T_{\text{Box}} C_{\text{ant}}$  term,  
 601  $\varepsilon_G T_{\text{Box}} C_{\text{ant}}$ , according to Ganachaud et al. (2000), such as:

$$602 \quad \varepsilon_G T_{\text{Box}} C_{\text{ant}} = \sum_{i=1}^{n \text{ layers}} \sqrt{4 \times \sigma_{T_{\text{Box}i}}^2 \times \text{std}(C_{\text{ant}i})^2} = 5 \text{ kmols}^{-1}$$

603 Where  $\varepsilon_G T_{\text{Box}} C_{\text{an}}$  was given as the sum of the tracer transport uncertainties by horizontal layers. In  
 604 the equation, the factor 4 aims to account for possible correlations between the zonal average and  
 605 horizontal eddy component (Ganachaud et al., 2000).

### 606 A.3. Robustness of $C_{\text{ant}}$ transports: perturbation analysis

607 In section A2, the uncertainty estimates were based on the assumption that errors are  
 608 independent of one another. As this assumption may be questionable, we performed a perturbation  
 609 analysis of uncertainties (Lawson and Hanson, 1974) to validate whether uncertainties were being  
 610 underestimated and, at the same time, to check the robustness of our results. Final uncertainties  
 611 were computed here as the standard deviation of an ensemble generated by random perturbation  
 612 of the  $C_{\text{ant}}$  transports.

#### 613 A.3.1. Perturbed $C_{\text{ant}}$ transports

614 As shown in equation (1), the transport of  $C_{\text{ant}}$  comes from the combination (product) of  
 615 the absolute velocities and  $C_{\text{ant}}$  concentrations. Both data fields are obtained following two  
 616 different methodologies: *i*) water property inversion estimating the volumetric transports (in this  
 617 study, a result by Carracedo et al. 2014); and *ii*) back-calculation of  $C_{\text{ant}}$  based on water properties

618 (as explained in A.1). If, in addition, we want to provide the  $C_{\text{ant}}$  transport by water mass, as shown  
 619 in equation (3), a third factor takes part: the water mass mixing fractions, obtained by means of an  
 620 OMP analysis (in this study, a result by Carracedo et al. 2014).

621 The procedure followed for the perturbation analysis consisted of re-computing the transport  
 622 of  $C_{\text{ant}}$  from 100 randomly perturbed fields of velocity,  $C_{\text{ant}}$  and water fractions (test 1). To test  
 623 which of the perturbed fields (velocity,  $C_{\text{ant}}$  or water masses fractions) influences the results the  
 624 most, we also re-estimated the  $C_{\text{ant}}$  transports by perturbing just one of the factors each time, that  
 625 is, we estimated the  $C_{\text{ant}}$  transports:

- 626 a) test 2: from 100 randomly perturbed velocity fields (no perturbed  $C_{\text{ant}}$  or water mass fractions)
- 627 b) test 3: from 100 randomly perturbed  $C_{\text{ant}}$  fields (no perturbed velocities or water mass fractions  
 628 (test 3))
- 629 c) test 4: from 100 randomly perturbed water mass fractions (no perturbed velocities or  $C_{\text{ant}}$ )

630 To perturb any of the variables, we assumed they followed a normal distribution, so that the  
 631 perturbation process lay in varying the property values according to a normal distribution within a  
 632 given range.

633 As for the velocity field, we based on the inverse model surface-to-bottom mass conservation  
 634 constraint ( $\text{Tr}_{\text{net}}=0.01 \pm 1$  Sv, Carracedo et al. 2014), to ensure the perturbed velocity field was  
 635 consistent with mass conservation. We randomly perturbed the net volume transport across the  
 636 section with zero mean and standard deviation of 1 Sv, obtaining a cross-section perturbed velocity  
 637  $v_p$  of:  $v_p = (\text{Tr}_{\text{net}})_{\text{perturbed}} / \text{total section area}$ . This velocity was (zonally and vertically) uniformly  
 638 added to the velocity field, so that the perturbed velocity field was still consistent with mass  
 639 conservation.

640  $C_{\text{ant}}$  concentrations were randomly perturbed with zero mean and standard deviation of  $5.2 \mu\text{mol}$   
 641  $\text{kg}^{-1}$ , being  $5.2 \mu\text{mol kg}^{-1}$  the overall uncertainty for the  $C_{\text{ant}}$  estimates (Vázquez-Rodríguez et al.,  
 642 2009b).

643 As for the water mixing fractions, both the properties of each water sample and of each source  
 644 water type (also referred to as source water mass, SWM) were perturbed. In terms of the OMP  
 645 analysis, the SWMs are points in the  $n$ -dimensional parameter space ( $n$  is the number of properties  
 646 that characterize SWMs) (Tomczak, 1981). In the study of Carracedo et al. (2014), the SWMs were  
 647 characterized by  $\theta$ , S,  $\text{O}_2^0$ ,  $\text{NO}_3^0$ ,  $\text{PO}_4^0$  and  $\text{Si}(\text{OH})_4^0$  (where the superscript 0 means preformed  
 648 variables) (see Table A2). The properties of each SWM were randomly modified with the mean  
 649 being the value of the property, and the standard deviation (STD), the values given by Álvarez et  
 650 al (2005) for  $\theta$  and S, and a percentage of their value for  $\text{O}_2$  (1% of the property value) and  
 651 nutrients (2% of the property value) (Table A2). The perturbation of the water sample properties  
 652 were performed with the mean equal to the property value at each point and the standard deviation  
 653 equal to the accuracy of each water sample property ( $\epsilon$ , Table A2). 100 perturbations were done  
 654 and the OMP analysis was solved for each perturbed system. Uncertainties for the SWMs  
 655 contributions were computed as the standard deviation of the 100 water mass distribution matrices.  
 656 The mean standard distribution (referred to as uncertainty) is shown in Table A2.

657 Table A2. Main properties of each of the Source Water Masses (SWMs) considered in the eOMP  
 658 analysis by Carracedo et al. (2014), with their correspondent standard deviation (STD). Note that



659 what we refer to as Central Waters (CW) in the present study is the sum of MMW, ENACW<sub>T</sub> and  
 660 ENACW<sub>P</sub>. Accuracies of the measured properties,  $\varepsilon$ , used to compute the perturbation of the tracer  
 661 fields are also shown. The last column accounts for the uncertainties in the SWMs contributions,  
 662 that is, the mean of the standard deviation of the 100 perturbations (values expressed on a per one  
 663 basis).

	Potential Temperature ( $\theta^{SWT}$ )	Salinity ( $S^{SWT}$ )	Silicate ( $Si(OH)_4^0$ <sub>SWT</sub> )	Nitrate ( $NO_3^0$ <sub>SWT</sub> )	Phosphate ( $PO_4^0$ <sub>SWT</sub> )	Oxygen ( $O_2$ <sub>SWT</sub> )	Uncertainty
	$^{\circ}C$	<i>psu</i>	$\mu mol\ kg^{-1}$				<i>Parts per unit</i>
MMW	20.0±0.5	37.00±0.04	0±0	0±0	0±0	223±2	0.03
ENACW <sub>T</sub>	15.3±0.4	36.10±0.02	2.05±0.04	1.23±0.02	0.136±0.003	244±2	0.04
ENACW <sub>P</sub>	8.3±0.3	35.23±0.01	9.8±0.2	11.1±0.2	1.10±0.02	304±3	0.05
MW	11.7±0.1	36.50±0.01	9.1±0.2	4.0±0.1	0.31±0.01	261±3	0.02
AAIW	7.5±0.1	35.00±0.02	24.8±0.5	16.2±0.3	0.95±0.02	290±3	0.04
LSW	3.4±0.2	34.89±0.12	9.1±0.2	12.5±0.2	0.94±0.02	325±3	0.03
ISOW	2.5±0.1	34.98±0.02	13.8±0.3	7.1±0.1	0.60±0.01	319±3	0.01
NEADW <sub>L</sub>	1.920±0.003	34.885±0.002	50.0±1.0	13.6±0.3	0.95±0.02	337±3	0.02
$\varepsilon$	0.005	0.005	0.5	0.2	0.002	3.3	-

664 To illustrate the results of the perturbation analysis, we recomputed as an example the net  
 665  $C_{ant}$  transport across the section,  $T_{Box}C_{ant}$ , for the 4 different tests (100 perturbations each test) and  
 666 calculated the standard deviation of the 100 values per test (see Table A3). More than 80% of the  
 667  $C_{ant}$  transport error estimate is due to the velocity field, whereas  $C_{ant}$  concentration uncertainty just  
 668 accounts for less than 20% of the total error. If we consider the  $C_{ant}$  transport by water masses,  
 669 then the water masses contribution accounts for around 65% of the total error, velocity field for  
 670 25% and  $C_{ant}$  concentrations for 10-15%.

671 By comparing the uncertainty estimates from the perturbation analysis with the uncertainty  
 672 estimates from the error propagation formula (as explained in Section A2), we see the former are  
 673 smaller than the latter. In view of that, we took the uncertainties obtained by error propagation,  
 674 that is, the largest ones, as those accompanying our results in the manuscript.

675 Table A3. Standard deviation of the 100-times perturbed net  $C_{ant}$  transports for each of the 4 tests  
 676 performed. In parenthesis, percentage of the total uncertainty represented by each of the variables  
 677 ( $v$ ,  $C_{ant}$  or WMs).  $v$  refers to the velocity field,  $C_{ant}$  to the  $C_{ant}$  concentrations; WMs to the water  
 678 masses contribution; CW to Central waters; MW to Mediterranean Water.

<i>Perturbation Analysis</i>			
Perturbed field	Net $C_{ant}$ transport		
	(kmol/s)		
	Total	Net by CW	Net by MW
test 1: $v$ , $C_{ant}$ , WMs	± 4	± 3	± 1

test 2:	$\nu$	$\pm 4$ (82%)	$\pm 1$ (22%)	$\pm 0.5$ (27%)
test 3:	$C_{\text{ant}}$	$\pm 0.8$ (18%)	$\pm 0.6$ (14%)	$\pm 0.1$ (7%)
test 4:	WMs	-	$\pm 3$ (64%)	$\pm 1$ (65%)
<i>Error Propagation</i>				
(see A.2)		$\pm 14$	$\pm 18$	$\pm 8$

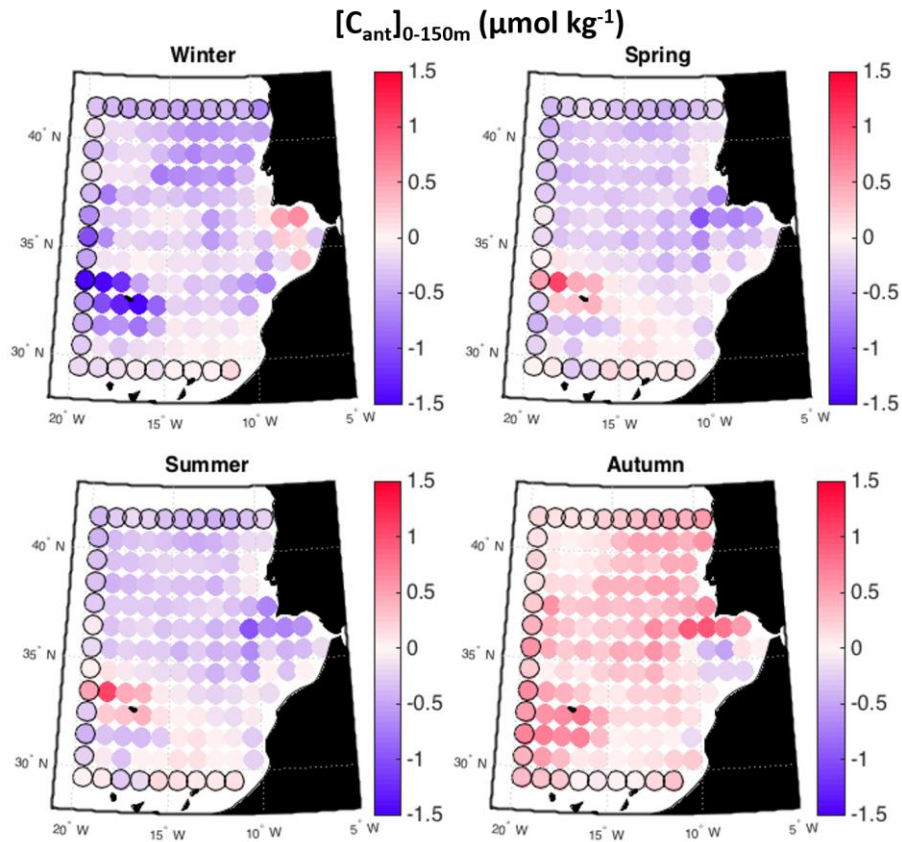
679 A.3.2. Perturbed Air-sea  $C_{\text{ant}}$  flux

680  $F_{\text{Air-sea}}C_{\text{ant}}$  is estimated (Eq. 6) as the difference between the  $C_{\text{ant}}$  storage rate and the  $C_{\text{ant}}$   
681 being advected across the walls of the enclosed box ( $T_{\text{Box}}C_{\text{ant}} + T_{\text{Strait}}C_{\text{ant}}$ ). Therefore, the  
682 perturbation procedure consisted in re-estimating  $F_{\text{Air-sea}}C_{\text{ant}}$  by perturbing independently each of  
683 the terms to be summed up as follows: i)  $C_{\text{ant}}$  storage rate: We recomputed the  $C_{\text{ant}}$  inventory by  
684 randomly perturbing  $C_{\text{ant}}$  concentrations according to a normal distribution with zero mean and  
685 standard deviation of  $5.2 \mu\text{mol kg}^{-1}$  (Vázquez-Rodríguez et al., 2009b); ii)  $T_{\text{Box}}C_{\text{ant}}$ : We used the  
686 estimates from the “test 1” perturbation analysis (see previous section); iii)  $T_{\text{Strait}}C_{\text{ant}}$ : we randomly  
687 perturbed this value by following a normal distribution with mean  $11 \text{ kmol s}^{-1}$  and standard  
688 deviation  $1 \text{ kmol s}^{-1}$ .

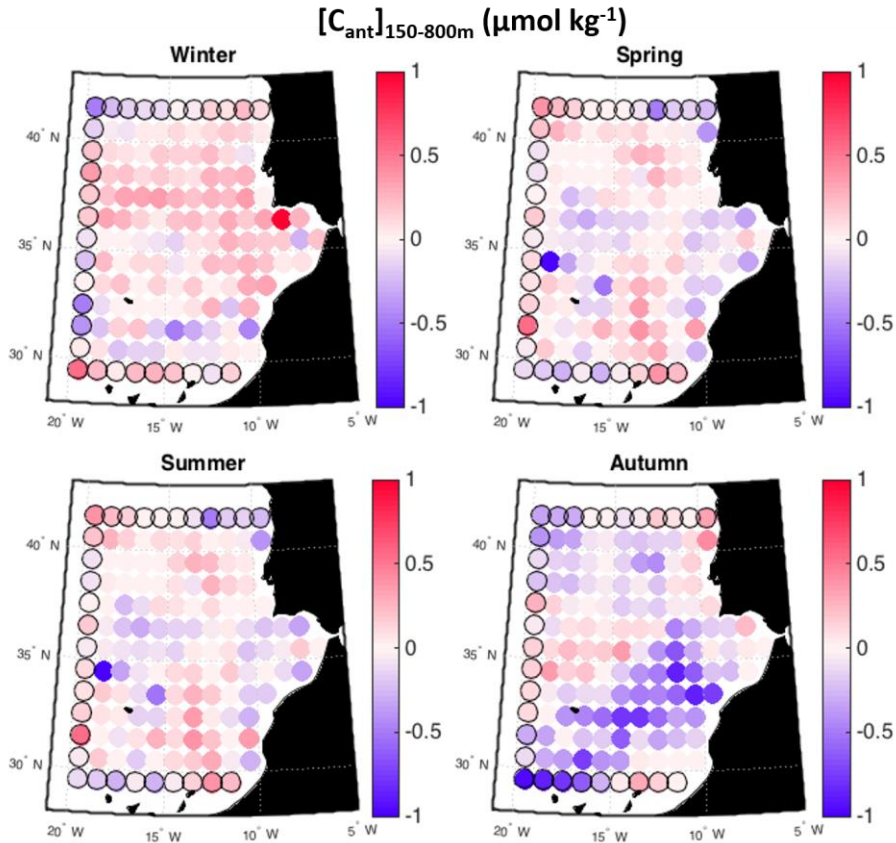
689 The standard deviation of the ensemble of 100  $F_{\text{Air-sea}}C_{\text{ant}}$  estimates was  $4 \text{ kmol s}^{-1}$ , an  
690 uncertainty smaller than that obtained by error propagation ( $10 \text{ kmol s}^{-1}$ , section A2.3). So once  
691 again, we kept the largest uncertainty as the most suitable one.

692 **Appendix B. Supplementary Figures**

693 Supplementary figures associated with this article can be found in the online version.



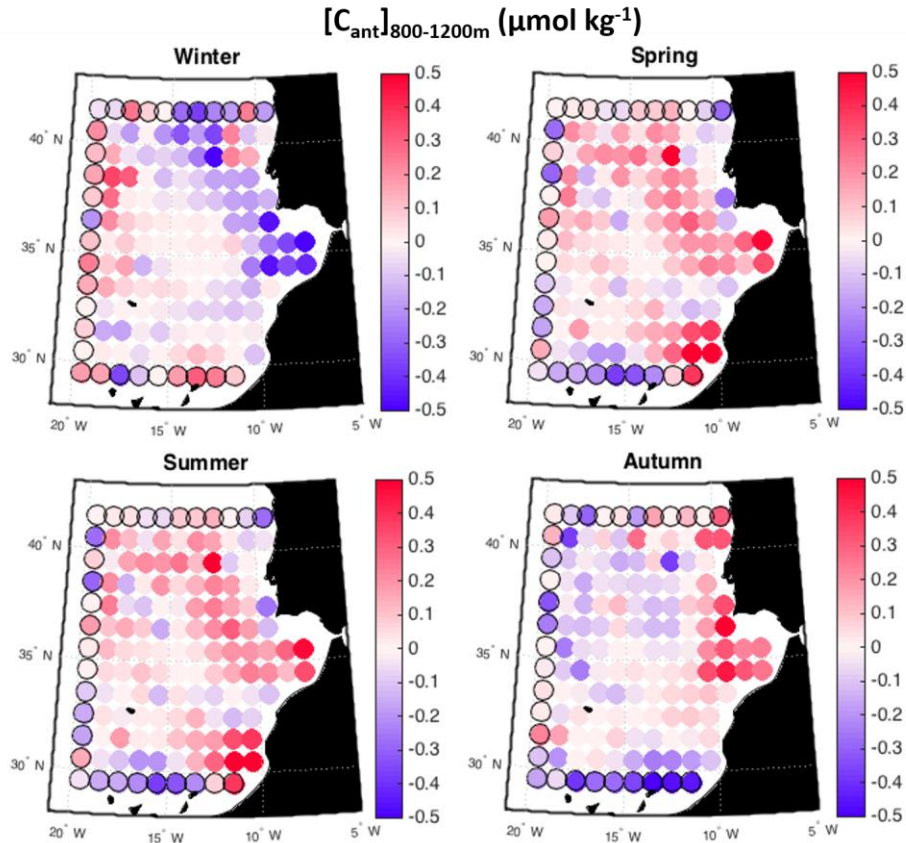
694 **Figure B1. a)** Seasonal distribution maps of  $C_{ant}$  anomalies in the upper 150 m of the water  
 695 column. Anomalies are estimated as the seasonal  $C_{ant}$  concentration averaged in the upper 150 m  
 696 minus the annual  $C_{ant}$  concentration averaged in the upper 150 m.  
 697  
 698



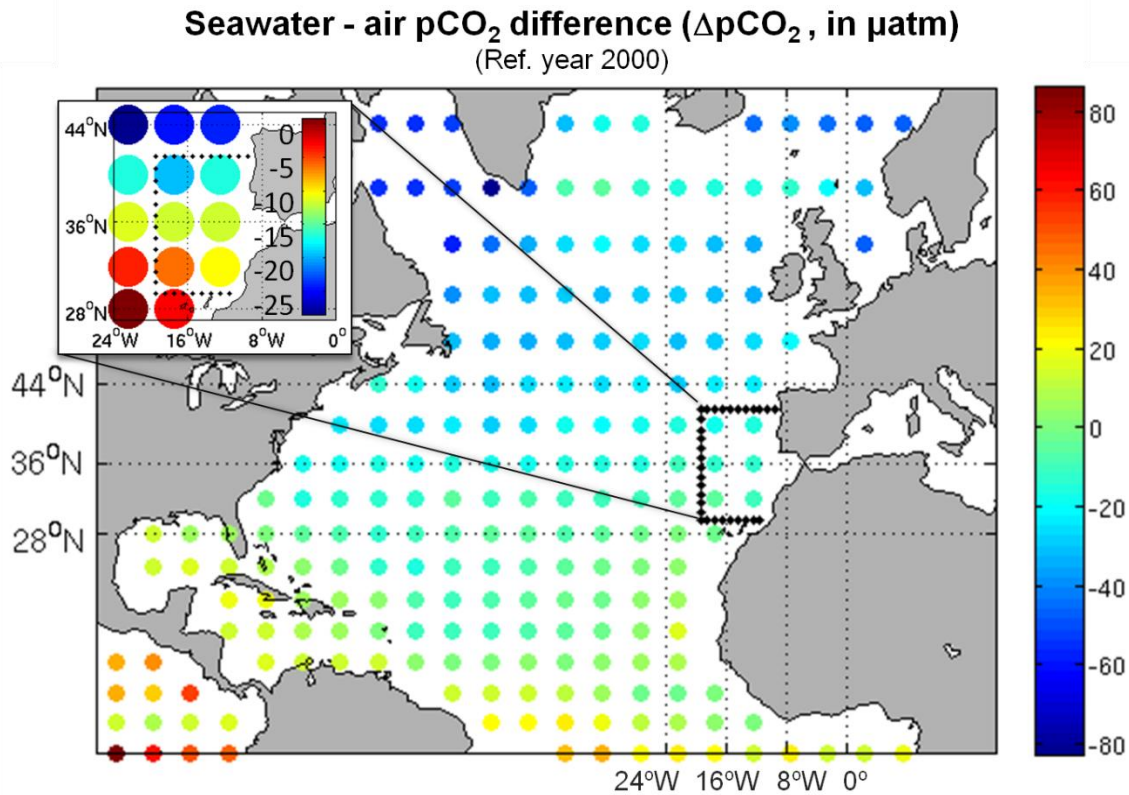
699  
700  
701  
702

**Figure B1. b)** Seasonal distribution maps of  $C_{\text{ant}}$  anomalies between 150-800 m. Anomalies are estimated as the seasonal  $C_{\text{ant}}$  concentration averaged between 150-800 m minus the annual  $C_{\text{ant}}$  concentration averaged between 150-800 m.



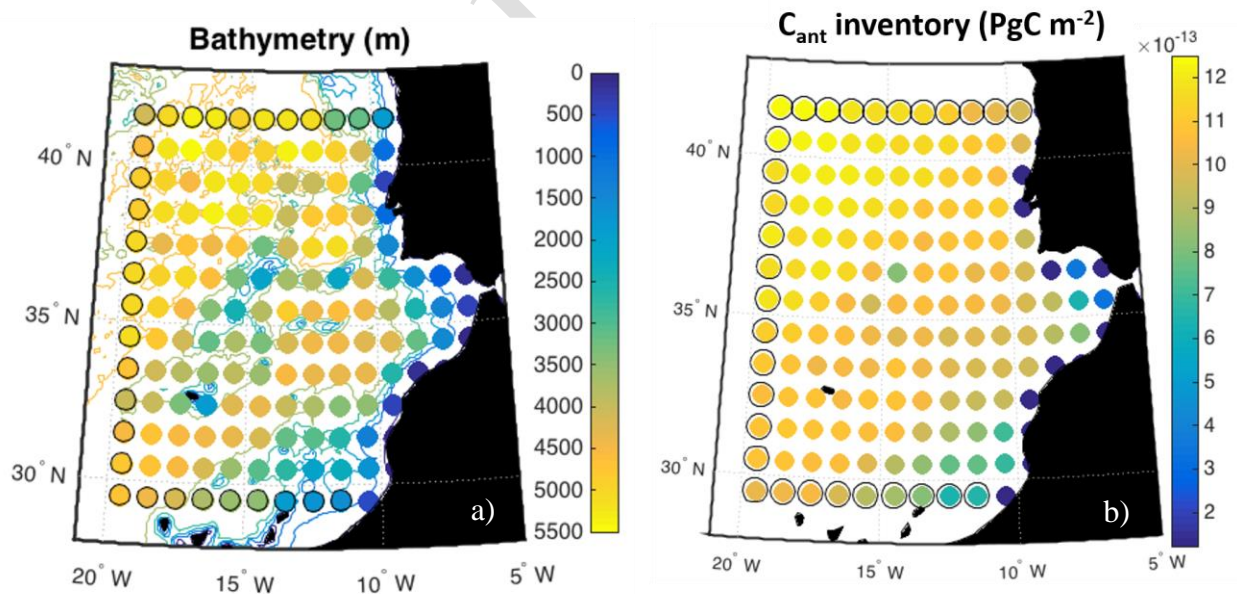


703  
704 **Figure B1. c)** Seasonal distribution maps of  $C_{\text{ant}}$  anomalies between 800-1200 m. Anomalies are  
705 estimated as the seasonal  $C_{\text{ant}}$  concentration averaged between 800-1200 m minus the annual  $C_{\text{ant}}$   
706 concentration averaged between 800-1200 m.



707  
708  
709  
710

**Figure B2.** Distribution maps of the climatological annual mean of the air-sea difference in CO<sub>2</sub> partial pressure (4° Latitude x 5° Longitude).



711  
712  
713

**Figure B3.** a) Averaged bathymetry (m) by grid node; b) Distribution of the area-normalized  $C_{\text{ant}}$  inventory ( $\text{Pg-C m}^{-2}$ ).

714 **References**

- 715 Aït-Ameur, N., Goyet, C., 2006. Distribution and transport of natural and anthropogenic CO<sub>2</sub> in  
716 the Gulf of Cadiz. *Deep Sea Res. Part II Top. Stud. Oceanogr.*, The Gulf of Cadiz  
717 Oceanography: A Multidisciplinary View The Gulf of Cadiz Oceanography: A  
718 Multidisciplinary View 53, 1329–1343. doi:10.1016/j.dsr2.2006.04.003.
- 719 Álvarez, M., Pérez, F.F., Shoosmith, D.R., Bryden, H.L., 2005. Unaccounted role of  
720 Mediterranean Water in the drawdown of anthropogenic carbon. *J. Geophys. Res.* 110.  
721 doi:10.1029/2004JC002633
- 722 Anderson, L.A., Sarmiento, J.L., 1994. Redfield ratios of remineralization determined by nutrient  
723 data analysis. *Glob. Biogeochem Cycles* 8, 65–80. doi:10.1029/93GB03318.
- 724 Barbosa Aguiar, A.C., Péliz, A., Neves, F., Bashmachnikov, I., Carton, X., 2015. Mediterranean  
725 outflow transports and entrainment estimates from observations and high-resolution  
726 modelling. *Prog. Oceanogr.* 131, 33–45. doi:10.1016/j.pocean.2014.11.008.
- 727 Benson, B.B., Krause, D., 1984. The concentration and isotopic fractionation of oxygen  
728 dissolved in freshwater and seawater in equilibrium with the atmosphere. *Limnol.*  
729 *Oceanogr.* 29, 620–632.
- 730 Boyer, T.P., Antonov, J.I., Baranova, O.K., Garcia, H.E., Johnson, D.R., Locarnini, R.A.,  
731 Mishonov, A.V., Seidov, D., Smolyar, I.V., Zweng, M.M., 2009. *World Ocean Database*  
732 2009, Chapter 1: Introduction, Levitus, S. ed. Washington, D. C.
- 733 Brewer, P.G., 1978. Direct observation of the oceanic CO<sub>2</sub> increase. *Geophys. Res. Lett.* 5, 997–  
734 1000. doi:10.1029/GL005i012p00997
- 735 Broecker, W.S., 1974. “NO”, a conservative water-mass tracer. *Earth Planet. Sci. Lett.* 23, 100–  
736 107. doi:10.1016/0012-821X(74)90036-3.
- 737 Carracedo, L.I., Gilcoto, M., Mercier, H., Pérez, F.F., 2014. Seasonal dynamics in the Azores–  
738 Gibraltar Strait region: A climatologically-based study. *Prog. Oceanogr.* 122, 116–130.  
739 doi:10.1016/j.pocean.2013.12.005.
- 740 Carracedo, L.I., Gilcoto, M., Mercier, H., Pérez, F.F., 2015. Quasi-synoptic transport, budgets  
741 and water mass transformation in the Azores–Gibraltar Strait region during summer  
742 2009. *Prog. Oceanogr.* 130, 47–64. doi:10.1016/j.pocean.2014.09.006.
- 743 Carracedo, L.I., Pardo, P.C., Flecha, S., Pérez, F.F., 2016. On the Mediterranean Water  
744 Composition. *J. Phys. Oceanogr.* 46, 1339–1358. doi:10.1175/JPO-D-15-0095.1.
- 745 Chen, G.T., Millero, F.J., 1979. Gradual increase of oceanic CO<sub>2</sub>. *Nature* 277, 205–206.  
746 doi:10.1038/277205a0
- 747 Fajar, N.M., Pardo, P.C., Carracedo, L., Vázquez-Rodríguez, M., Ríos, A.F., Pérez, F.F., 2012.  
748 Trends of anthropogenic CO<sub>2</sub> along 20° W in the Iberian Basin. *Cienc. Mar.* 38, 287–306.
- 749 Fajar, N.M., Guallart, E.F., Steinfeldt, R., Ríos, A.F., Pelegrí, J.L., Pelejero, C., Calvo, E., Pérez,  
750 F.F., 2015. Anthropogenic CO<sub>2</sub> changes in the Equatorial Atlantic Ocean. *Prog.*  
751 *Oceanogr.* 134, 256–270. doi:10.1016/j.pocean.2015.02.004.
- 752 Flecha, S., Pérez, F.F., Navarro, G., Ruiz, J., Olivé, I., Rodríguez-Gálvez, S., Costas, E., Huertas,  
753 I.E., 2012. Anthropogenic carbon inventory in the Gulf of Cadiz. *J. Mar. Syst.* 92, 67–75.  
754 doi:10.1016/j.jmarsys.2011.10.010.
- 755 Fusco, G., Artale, V., Cotroneo, Y., Sannino, G., 2008. Thermohaline variability of  
756 Mediterranean Water in the Gulf of Cadiz, 1948–1999. *Deep Sea Res. Part Oceanogr.*  
757 *Res. Pap.* 55, 1624–1638. doi:10.1016/j.dsr.2008.07.009.

- 758 Ganachaud, A., Wunsch, C., Marotzke, J., Toole, J., 2000. Meridional overturning and large-  
 759 scale circulation of the Indian Ocean. *J. Geophys. Res.* 105, 26117–26,134.  
 760 doi:10.1029/2000JC900122.
- 761 Gruber, N., Sarmiento, J.L., Stocker, T.F., 1996. An improved method for detecting  
 762 anthropogenic CO<sub>2</sub> in the oceans. *Glob. Biogeochem. Cycles* 10, 809–837.  
 763 doi:10.1029/96GB01608
- 764 Huertas, I.E., Ríos, A.F., García-Lafuente, J., Makaoui, A., Rodríguez-Gálvez, S., Sánchez-  
 765 Román, A., Orbi, A., Ruiz, J., Pérez, F.F., 2009. Anthropogenic and natural CO<sub>2</sub>  
 766 exchange through the Strait of Gibraltar.
- 767 Keeling, C.D., Bolin, B., 2010. The simultaneous use of chemical tracers in oceanic studies I.  
 768 General theory of reservoir models 1,2. *Tellus* 19, 566–581. doi:10.1111/j.2153-  
 769 3490.1967.tb01509.x.
- 770 Key, R.M., Olsen, A., van Heuven, S., Lauvset, S.K., Velo, A., Lin, X., Schirnack, C., Kozyr, A.,  
 771 Tanhua, T., Hoppema, M., Jutterstrom, S., Steinfeldt, R., Jeansson, E., Ishi, M., Perez,  
 772 F.F., Suzuki, T., 2015. Global Ocean Data Analysis Project, Version 2 (GLODAPv2),  
 773 ORNL/CDIAC-162, ND-P093. Carbon Dioxide Information Analysis Center (CDIAC).
- 774 Le Quéré, C., Moriarty, R., Andrew, R.M., Canadell, J.G., Sitch, S., Korsbakken, J.I.,  
 775 Friedlingstein, P., Peters, G.P., Andres, R.J., Boden, T.A., Houghton, R.A., House, J.I.,  
 776 Keeling, R.F., Tans, P., Arneeth, A., Bakker, D.C.E., Barbero, L., Bopp, L., Chang, J.,  
 777 Chevallier, F., Chini, L.P., Ciais, P., Fader, M., Feely, R.A., Gkritzalis, T., Harris, I.,  
 778 Hauck, J., Ilyina, T., Jain, A.K., Kato, E., Kitidis, V., Klein Goldewijk, K., Koven, C.,  
 779 Landschützer, P., Lauvset, S.K., Lefèvre, N., Lenton, A., Lima, I.D., Metzl, N., Millero,  
 780 F., Munro, D.R., Murata, A., Nabel, J.E.M.S., Nakaoka, S., Nojiri, Y., O'Brien, K.,  
 781 Olsen, A., Ono, T., Pérez, F.F., Pfeil, B., Pierrot, D., Poulter, B., Rehder, G., Rödenbeck,  
 782 C., Saito, S., Schuster, U., Schwinger, J., Séférian, R., Steinhoff, T., Stocker, B.D.,  
 783 Sutton, A.J., Takahashi, T., Tilbrook, B., van der Laan-Luijkx, I.T., van der Werf, G.R.,  
 784 van Heuven, S., Vandemark, D., Viovy, N., Wiltshire, A., Zaehle, S., Zeng, N., 2015.  
 785 Global Carbon Budget 2015. *Earth Syst. Sci. Data* 7, 349–396. doi:10.5194/essd-7-349-  
 786 2015.
- 787 Lee, K., Choi, S.D., Park, G.H., Wanninkhof, R., Peng, T.H., Key, R.M., Sabine, C.L., Feely,  
 788 R.A., Bullister, J.L., Millero, F.J., 2003. An updated anthropogenic CO<sub>2</sub> inventory in the  
 789 Atlantic Ocean. *Glob. Biogeochem. Cycles* 17, 1116. doi:10.1029/2003GB002067.
- 790 Lønborg, C., Álvarez-Salgado, X.A., 2014. Tracing dissolved organic matter cycling in the  
 791 eastern boundary of the temperate North Atlantic using absorption and fluorescence  
 792 spectroscopy. *Deep Sea Res. Part Oceanogr. Res. Pap.* 85, 35–46.  
 793 doi:10.1016/j.dsr.2013.11.002.
- 794 Mercier, H., 1986. Determining the general circulation of the ocean: A nonlinear inverse  
 795 problem. *J. Geophys. Res. Oceans* 91, 5103–5109.
- 796 Olsen, A., Key, R.M., van Heuven, S., Lauvset, S.K., Velo, A., Lin, X., Schirnack, C., Kozyr, A.,  
 797 Tanhua, T., Hoppema, M., Jutterström, S., Steinfeldt, R., Jeansson, E., Ishii, M., Pérez,  
 798 F.F., Suzuki, T., 2016. The Global Ocean Data Analysis Project version 2 (GLODAPv2)  
 799 – an internally consistent data product for the world ocean. *Earth Syst. Sci. Data* 8, 297–  
 800 323. doi:10.5194/essd-8-297-2016.
- 801 Pardo, P.C., Pérez, F.F., Velo, A., Gilcoto, M., 2012. Water masses distribution in the Southern  
 802 Ocean: Improvement of an extended OMP (eOMP) analysis. *Prog. Oceanogr.* 103, 92–  
 803 105. doi:10.1016/j.pocean.2012.06.002.



- 804 Pérez, F.F., Vázquez-Rodríguez, M., Louarn, E., Padín, X.A., Mercier, H., Ríos, A.F., 2008.  
 805 Temporal variability of the anthropogenic CO<sub>2</sub> storage in the Irminger Sea.  
 806 *Biogeosciences* 5, 1669–1679.
- 807 Pérez, F.F., Arístegui, J., Vázquez-Rodríguez, M., Ríos, A.F., 2010. Anthropogenic CO<sub>2</sub> in the  
 808 Azores region. *Sci. Mar.* 74, 11–19. doi:10.3989/scimar.2010.74s1011.
- 809 Pérez, F.F., Mercier, H., Vázquez-Rodríguez, M., Lherminier, P., Velo, A., Pardo, P.C., Rosón,  
 810 G., Ríos, A.F., 2013. Atlantic Ocean CO<sub>2</sub> uptake reduced by weakening of the  
 811 meridional overturning circulation. *Nat. Geosci.* 6, 146–152. doi:10.1038/ngeo1680.
- 812 Quay, P., Sonnerup, R., Stutsman, J., Maurer, J., Körtzinger, A. Padin, X. A., Robinson, C.,  
 813 2007. Anthropogenic CO<sub>2</sub> accumulation rates in the North Atlantic Ocean from changes  
 814 in the <sup>13</sup>C/<sup>12</sup>C of dissolved inorganic carbon. *Global Biogeochem. Cycles*, 21, GB1009.  
 815 doi:10.1029/2006GB002761.
- 816 Rhein, M., Rintoul, S.R., Aoki, S., Campos, E., Chambers, D., Feely, R.A., Gulev, S., Johnson,  
 817 G.C., Josey, S.A., Kostianoy, A., Mauritzen, C., Roemmich, D., Talley, L.D., Wang, F.,  
 818 2013. Observations: Ocean, in: *Climate Change 2013: The Physical Science Basis.*  
 819 Contribution of Working Group I to the Fifth Assessment Report of the  
 820 Intergovernmental Panel on Climate Change. [Stocker, T.F., D. Qin, G.-K. Plattner, M.  
 821 Tignor, S.K. Allen, J. Boschung, A. Nauels, Y. Xia, V. Bex and P.M. Midgley (Eds.)].  
 822 Cambridge University Press, Cambridge, United Kingdom and New York, NY, USA.  
 823 Cambridge University Press, Cambridge, Uited Kingdom and New York, NY, USA, pp.  
 824 255–316.
- 825 Ribas-Ribas, M., Gómez-Parra, A., Forja, J.M., 2011. Air–sea CO<sub>2</sub> fluxes in the north-eastern  
 826 shelf of the Gulf of Cadiz (southwest Iberian Peninsula). *Mar. Chem.* 123, 56–66.  
 827 doi:10.1016/j.marchem.2010.09.005.
- 828 Ríos, A.F., Pérez, F.F., Fraga, F., 2001. Long-term (1977–1997) measurements of carbon dioxide  
 829 in the Eastern North Atlantic: evaluation of anthropogenic input. *Deep Sea Res. Part II*  
 830 *Top. Stud. Oceanogr.*, JGOFS Research in the North Atlantic Ocean: A Decade of  
 831 Research, Synthesis and modelling 48, 2227–2239. doi:10.1016/S0967-0645(00)00182-  
 832 X.
- 833 Ríos, A.F., Vázquez-Rodríguez, M., Padín, X.A., Pérez, F.F., 2010. Anthropogenic carbon  
 834 dioxide in the South Atlantic western basin. *J. Mar. Syst.* 83, 38–44.  
 835 doi:10.1016/j.jmarsys.2010.06.010.
- 836 Ríos, A.F., Velo, A., Pardo, P.C., Hoppema, M., Pérez, F.F., 2012. An update of anthropogenic  
 837 CO<sub>2</sub> storage rates in the western South Atlantic basin and the role of Antarctic Bottom  
 838 Water. *Journal of Marine Systems* 94, 197–203.
- 839 Ríos, A. F., Resplandy, L., García-Ibáñez, M. I., Fajar, N. M., Velo, A., Padin, X. A., Pérez, F.  
 840 F., 2015. Decadal acidification in the water masses of the Atlantic Ocean. *Proceedings of*  
 841 *the National Academy of Sciences of the United States of America*, 112(32), 9950–9955.  
 842 <http://doi.org/10.1073/pnas.1504613112>.
- 843 Sabine, C.L., Feely, R.A., Gruber, N., Key, R.M., Lee, K., Bullister, J.L., Wanninkhof, R., Wong,  
 844 C.S., Wallace, D.W.R., Tilbrook, B., Millero, F.J., Peng, T.-H., Kozyr, A., Ono, T., Rios,  
 845 A.F., 2004. The Oceanic Sink for Anthropogenic CO<sub>2</sub>. *Science* 305, 367–371.  
 846 doi:10.1126/science.1097403.
- 847 Soto-Navarro, J., Criado-Aldeanueva, F., García-Lafuente, J., Sánchez-Román, A., 2010.  
 848 Estimation of the Atlantic inflow through the Strait of Gibraltar from climatological and  
 849 in situ data. *J. Geophys. Res.* 115. doi:10.1029/2010JC006302.

- 850 Speth, P., Detlefsen, H., Sierts, H.-W., 1978. Meteorological influence on upwelling off  
851 Northwest Africa. *Dtsch. Hydrogr. Z.* 31, 95–104. doi:10.1007/BF02227007.
- 852 Steinfeldt, R., Rhein, M., Bullister, J.L., Tanhua, T., 2009. Inventory changes in anthropogenic  
853 carbon from 1997–2003 in the Atlantic Ocean between 20°S and 65°N. *Glob.*  
854 *Biogeochem. Cycles* 23, GB3010. doi:10.1029/2008GB003311.
- 855 Stocker, T.F., Qin, D., Plattner, G.-K., Tignor, M., Allen, S.K., Boschung, J., Nauels, A., Xia, Y.,  
856 Bex, V., Midgley, P.M. (Eds.), 2013. *Climate Change 2013: The Physical Science Basis.*  
857 *Contribution of Working Group I to the Fifth Assessment Report of the Intergovernmental*  
858 *Panel on Climate Change.* Cambridge University Press, Cambridge, United Kingdom and  
859 New York, NY, USA.
- 860 Takahashi, T., Broecker, W.S., Langer, S., 1985. Redfield ratio based on chemical data from  
861 isopycnal surfaces. *J. Geophys. Res.* 90, 6907–6924. doi:10.1029/JC090iC04p06907.
- 862 Takahashi, T., Sutherland, S.C., Wanninkhof, R., Sweeney, C., Feely, R.A., Chipman, D.W.,  
863 Hales, B., Friederich, G., Chavez, F., Sabine, C., 2009. Climatological mean and decadal  
864 change in surface ocean pCO<sub>2</sub> and net sea–air CO<sub>2</sub> flux over the global oceans. *Deep Sea*  
865 *Res. Part II Top. Stud. Oceanogr.* 56, 554–577.
- 866 Tanhua, T., Biastoch, A., Körtzinger, A., Lüger, H., Böning, C., Wallace, D.W.R., 2006. Changes  
867 of anthropogenic CO<sub>2</sub> and CFCs in the North Atlantic between 1981 and 2004. *Glob.*  
868 *Biogeochem. Cycles* 20, 13 PP. doi:200610.1029/2006GB002695
- 869 Tomczak, M., 1981. A multi-parameter extension of temperature/salinity diagram techniques for  
870 the analysis of non-isopycnal mixing. *Prog. Oceanogr.* 10, 147–171.
- 871 van Aken, H.M., 2000. The hydrography of the mid-latitude Northeast Atlantic Ocean: II: The  
872 intermediate water masses. *Deep Sea Res. Part Oceanogr. Res. Pap.* 47, 789–824.  
873 doi:10.1016/S0967-0637(99)00112-0.
- 874 Vázquez-Rodríguez, M., Touratier, F., Lo Monaco, C., Waugh, D.W., Padín, X.A., Bellerby,  
875 R.G.J., Goyet, C., Metzl, N., Ríos, A.F., Pérez, F.F., 2009a. Anthropogenic carbon  
876 distributions in the Atlantic Ocean: data-based estimates from the Arctic to the Antarctic.  
877 *Biogeosciences* 6, 439–451.
- 878 Vázquez-Rodríguez, M., Padín, X.A., Ríos, A.F., Bellerby, R.G.J., Pérez, F.F., 2009b. An  
879 upgraded carbon-based method to estimate the anthropogenic fraction of dissolved CO<sub>2</sub> in  
880 the Atlantic Ocean. *Biogeosciences Discussions* 6, 4527–4571.  
881 <http://dx.doi.org/10.1016/j.jmarsys.2011.11.023>.
- 882 Vázquez-Rodríguez, M., Padín, X.A., Pardo, P.C., Ríos, A.F., Pérez, F.F., 2012. The subsurface  
883 layer reference to calculate preformed alkalinity and air–sea CO<sub>2</sub> disequilibrium in the  
884 Atlantic Ocean. *J. Mar. Syst.* 94, 52–63. doi:10.1016/j.jmarsys.2011.10.008.
- 885 Velo, A., Vázquez-Rodríguez, M., Padín, X.A., Gilcoto, M., Ríos, A.F., Pérez, F.F., 2010. A  
886 multiparametric method of interpolation using WOA05 applied to anthropogenic CO<sub>2</sub> in  
887 the Atlantic. *Sci. Mar.* 74, 21–32.
- 888 Watson, A.J., Schuster, U., Bakker, D.C.E., Bates, N.R., Corbiere, A., Gonzalez-Davila, M.,  
889 Friedrich, T., Hauck, J., Heinze, C., Johannessen, T., Kortzinger, A., Metzl, N., Olafsson,  
890 J., Olsen, A., Oschlies, A., Padin, X.A., Pfeil, B., Santana-Casiano, J.M., Steinhoff, T.,  
891 Telszewski, M., Rios, A.F., Wallace, D.W.R., Wanninkhof, R., 2009. Tracking the  
892 Variable North Atlantic Sink for Atmospheric CO<sub>2</sub>. *Science* 326, 1391–1393.  
893 doi:10.1126/science.1177394.

- 894 Woosley, R. J., Millero, F. J., Wanninkhof, R., 2016. Rapid anthropogenic changes in CO<sub>2</sub> and  
895 Ph in the Atlantic Ocean: 2003–2014. *Global Biogeochem. Cycles*, 30. doi:10.1002/  
896 2015GB005248.
- 897 Zunino, P., Garcia-Ibañez, M.I., Lherminier, P., Mercier, H., Rios, A.F., Pérez, F.F., 2014.  
898 Variability of the transport of anthropogenic CO<sub>2</sub> at the Greenland–Portugal OVIDE  
899 section: controlling mechanisms. *Biogeosciences* 11, 2375–2389. doi:10.5194/bg-11-  
900 2375-2014.

Author's Version